A pseudo thermo-mechanical model linking process parameters to microstructural evolution in multilayer additive friction stir deposition of magnesium alloy

Shashank Sharma, K.V. Mani Krishna, M. Radhakrishnan, Mangesh V. Pantawane, Shreyash M. Patil, Sameehan S. Joshi, Rajarshi Banerjee, Narendra B. Dahotre *

Department of Materials Science and Engineering, University of North Texas, 3940 N Elm St, Denton, TX 76207, USA
Center for Agile and Adaptive Additive Manufacturing, University of North Texas, 3940 N Elm St, Denton, TX 76207, USA

HIGHLIGHTS

- A multi-layer pseudo thermo-mechanical model considering frictional heating and plastic deformation have been developed for additive friction stir deposition.
- The pseudo thermo-mechanical model provides reasonable accuracy and computational efficiency (run time < 20 min for 5 layers).
- Simulations reveal the effect of process parameters (rotational speed, and traverse speed) on temperature and strain rates during AFSD.
- EBSD and TEM analysis suggested occurrence of dynamic recrystallization followed by grain coarsening during multi-layer depositions.
- Phenomenological relationship between Zener-Holloman parameter and grain size elucidates unique thermo-mechanical imprint on microstructure evolution during AFSD.

GRAPHICAL ABSTRACT
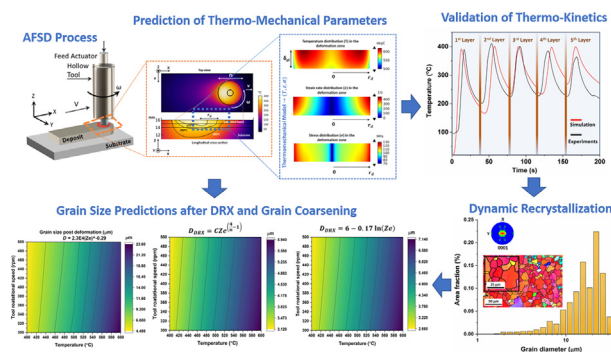
ARTICLE INFO

ABSTRACT

Additive friction stir deposition has been proposed as a disruptive manufacturing process; involving complex thermo-mechanical mechanisms during multilayer material deposition. The current efforts have attempted to develop a FEM based pseudo-mechanical thermal model accounting for heat generation due to friction and plastic dissipation during multilayer additive friction stir deposition. The primary motivation for development of the model was to seek an understanding of thermo-mechanical mechanisms and their impact on microstructural evolution during additive friction stir deposition. The predicted temperature–time profiles agreed well with the experimentally derived ones. The computational predictions indicate rise of the peak temperatures up to 0.8 times the melting temperature of Mg-alloy. In addition, the Zener-Holloman parameter, Ze evaluated using the computational model

---

* Corresponding author at: Department of Materials Science and Engineering, University of North Texas, 3940 N Elm St, Denton, TX 76207, USA.
 E-mail address: Narendra.Dahotre@unt.edu (N.B. Dahotre).

Nomenclature

E_s	Specific linear energy density (J/mm)	q_{loss}	Convective and radiative heat loss (W/m^2)
M	Tool Torque (Nm)	h_∞	Convective heat transfer coefficient to ambient (W/(m^{2}K))
ω	Tool rotational speed (rpm)		
V	Tool linear travel speed (mm/s)	ε	Emissivity of a material
r_s	Tool shoulder radius (mm)	σ	Stefan-Boltzmann coefficient (W/(m^{2}K^4))
r_d	Tool feed rod radius (mm)	T_∞	Ambient temperature (K or °C)
δ	Slip factor	η_{th}	Thermal efficiency
δ_{pl}	Plasticized layer thickness (mm)	σ_e	Equivalent stress (MPa)
ρ	Density (kg/m^3)	$\dot{\varepsilon}$	Equivalent strain rate (1/s)
C_p	Specific heat (J/(Kg*K))	σ_f	Flow stress (MPa)
$\vec{u}$	Advection velocity (mm/s)	σ_r	Material parameter (MPa)
k	Thermal conductivity (W/(m*K))	α	Material parameter
$Q'''_{plastic}$	Volumetric heat source due to plastic deformation (W/m^3)	m	Material parameter
		Ze	Zener-Holloman parameter (1/s)
T	Temperature (K or °C)	Q_{act}	Activation energy (kJ/mol)
q_f	Boundary heat flux due to frictional contact at feed rod/substrate interface (W/m^2)	R	Universal gas constant
		$\delta'_\varepsilon, \delta_\varepsilon$	Spatial adjustment scaler
τ_{yield}	Shear stress experienced by deformed material at feed rod (MPa)	z_i	Initial substrate coordinates
		R_l	Moving locus of the tool assembly in cartesian coordinates
θ	Angular displacement		
σ_{yield}	Yield strength of the material (MPa)	δ'_{pl}	Scaling constant
q_s	Boundary heat flux due to frictional contact at extruded material/substrate interface (W/m^2)	ND	AFSD sample thickness direction
		D_{DRX}	Dynamically recrystallized grain size
τ_{tool}	Shear stress experienced by deformed material at tool shoulder interface (MPa)	C	Fitting constant
		n	Stress exponent
η	Mechanical efficiency	D	Grain size after coarsening
δ_o	Scaling constant (<1)		
ω_o	Scaling constant reference for tool rotational speed		

Strain rate
Zener-Holloman parameter
Thermal model
Grain size
Microstructure
Dynamic recrystallization

was correlated with the microstructural evolution during the deposition process. The unique thermo-mechanical processing conditions during additive friction stir deposition led to dynamic recrystallization followed by grain coarsening. A significant extent of texture strengthening was observed in the AFSD processed samples. The already established phenomenological relationship between Ze and grain size was used to predict the grain size in the present work. The computational predictions indicate that the recrystallized grain size ranged from 4 to 6 μm, and the post deformation grain coarsening varied in the range of 4–24 μm, thereby providing reasonable agreement with the experimental observations.

1. Introduction

Additive friction stir deposition (AFSD) is a point of need disruptive manufacturing technology with the ability to print macro metal parts. Given its similarities with existing hot deformation processing techniques, AFSD is expected to result in considerable microstructural modifications and potentially superior mechanical properties of the deposited product. In AFSD, the feed rod material experiences frictional heating, thermal softening, compression, extrusion, and stirring, followed by deposition. Compared with existing friction-based manufacturing/ additive manufacturing (AM) methods, AFSD can be correlated to Continuous Drive Friction Welding (CDFW) such as friction stir welding/processing (FSW/FSP), rotary friction welding (RFW) and Friction surfacing (FS) [1–3]. The initial phase during AFSD, in which the rotating feed rod comes in contact with the substrate, results in frictional heating and thermal softening followed by plastic deformation, which is quite similar to RFW/FS. However, unlike RFW/FS, where the deformed material results in a flash, in AFSD the plasticized material is extruded between the tool-substrate gap and experiences extreme shearing similar to that in FSW. Thus, material deposited

during AFSD experiences intense thermo-mechanical history, thereby resulting in generation of unique microstructure [4,5].

Most importantly, AFSD is a layer-by-layer material deposition process where the thermo-mechanical phenomena repeat during deposition of each layer, thereby subjecting the deposited layers to cyclic and varying degrees of complex thermo mechanical process flows. Therefore, unlike FSW and RFW processes, AFSD entails a thermal cycling effect that profoundly affect the microstructural evolution during the deposition process. Thus, it is imperative to understand the thermo-mechanics and its possible consequences on microstructural evolution, ultimately establishing process-microstructure-property linkage in AFSD.

In literature, numerous attempts have been made to understand the complex thermo-mechanics of the friction-based manufacturing processes. These attempts can be classified into three different approaches (1) pure conduction-based thermal modeling [6–8], (2) computational fluid dynamics (CFD) [9–11] based material flow models, and 3) thermo-mechanically coupled computational solid dynamics models (CSM) [12–14]. The CFD and CSM models have attempted to incorporate pertinent physics of the friction-based manufacturing process, such as complex temperature-dependent

stress–strain relations during deformation, heat generation due to plastic deformation, and evolution of contact state (i.e., sliding or sticking mechanism) between tool/workpiece. Whereas thermal models offer a pseudo-mechanical approach where analytical estimation of frictional heat generation is solved to approximate temperature evolution during friction-based manufacturing process. In the context of AFSD, formulation of CFD or CSM-based techniques are challenging, as accommodation of extreme plastic deformation and layer-by-layer deposition is problematic in terms of meshing strategy for either Eulerian, Lagrangian, or coupled Eulerian-Lagrangian methodologies. Further, CFD or CSM simulation requires sophisticated computational resources and higher runtimes, rendering parametric variation studies rather cumbersome. Recently, a Smooth Particle Hydrodynamics-based AFSD model has been proposed, which alleviates the above challenges [15]. However, the model was restricted to a single-track deposition and the reported computational run time was substantially high (>30 hrs). Thus, there is a need for pure conduction-based multilayer thermal modeling in AFSD as a reasonable computationally efficient alternative. In light of this, in the present work a multilayer pseudo-mechanical thermal model for AFSD was developed. Furthermore, the thermal model was validated with experimentally acquired data during the AFSD. The primary motivation behind this work was to apply the validated thermal model in understanding the microstructural evolution during AFSD.

The material chosen for the present AFSD model was AZ31B Magnesium alloy. The primary reason of AZ31B as AFSD material was wide range of applications of magnesium-based alloys in automobile, aerospace, and biomedical industries [16–18]. In addition, Mg alloys have poor mechanical and formability characteristics due to their HCP crystal structure and associated lack of sufficient number of slip systems. Therefore, thermo-mechanical processing of Mg alloys (at high temperatures) has been explored immensely. Processes such as Equal Channel Angular Pressing (ECAP), uniaxial hot compression, tension, rolling, torsion, and more recently friction stir process have been employed to understand the formability and resulting microstructures of Mg alloys [19–22]. It has been observed that hot working of Mg alloys is conducive to grain refinement and weakening of (0002) fiber texture resulting in improvement in plastic anisotropy and ductility [21,23]. Recent studies have shown under varying thermo-mechanical processing conditions, AZ31B experienced dynamic recrystallization induced grain refinement, which resulted in exceptional mechanical properties [4,24]. Naturally, AFSD processing of AZ31B and its microstructural evolution warrants similar systematic investigation. Thus, in order to assess the thermomechanical response under extreme conditions of stress/strain coupled with the process generated high temperature in a process such as AFSD was considered in the present work. Such AFSD based processing also offers the advantage of grain refinement and associated enhancement in mechanical properties. Hence, AFSD based fabrication coupled with experimental-computational examination of AZ31 AFSD deposits require further exploration.

In light of this, the efforts presented in this manuscript dwelled on an integrated computational and experimental approach to understand the thermo-kinetics and thermo-mechanical mechanisms and associated microstructural evolution during AFSD of AZ31B. The numerical methodology with assumptions, governing equations, and respective boundary conditions have been explained. The thermo-mechanical evolution in terms of temperature, strain state, and state of stress during AFSD process have been elucidated. Lastly, it is demonstrated that the thermo-mechanical computational approach adapted in the present efforts has the ability to predict possible deformation mechanism, degree of recrystallization, and grain size approximation during AFSD of AZ31B.

2. Materials and methods

2.1. Experiments

A bar stock of 9.5x9.5 mm^2 cross-section and length of 460 mm was used during AFSD as a feed stock was machined/cut out of a commercially available of AZ31B Mg (Mg-3Al-1Zn-0.5Mn in wt%) plate of dimensions 9.5x460x460 mm^3. As per the material data sheet provided by the supplier, the AZ31B Mg plate (from which the feed stock was machined) was produced via wrought processing followed by H24 tempering (170–200 °C). AFSD was conducted on MELD® machine equipped with a hollow tool of 38.1 mm outer diameter and a coaxial cavity of dimensions 9.5x9.5x118 mm^3. Fig. 1 illustrates the schematic of the experimental setup used in this study. The feed stock was fed into the hollow AFSD tool and pushed down using actuator assembly against the AZ31B Mg base plate (substrate). While, the AFSD tool was rotated at a constant rotational velocity of 400 rpm, the tool linear velocity was varied in the range of 4.2–6.3 mm/s. A gap of ∼ 1 mm was maintained between rotating tool and the base plate surface with the help of tool protrusions (Fig. 1 (b-d)), to provide a room for the feed material to soften and shear during the deposition. Note that for the sake of visual aid, the tool protrusions are not illustrated in Fig. 1 (a), rather they are represented in the cross-sectional view (Fig. 1 (b-d)) with accurate spatial location. The tool was linearly translated to deposit a layer of dimension 140x40x1 mm^3. The tool was then displaced upward by 1 mm to deposit a successive layer. Total 5 layers were deposited under each set of AFSD process conditions.

It should be noted that, unlike other friction-based manufacturing processes (i.e., FSW, and CDFW), AFSD entails multiple physical processes such as feed rod deformation, material extrusion, stirring, and deposition. Understanding the chronology and interrelation of these physical processes is necessary to develop a thermal model. Accordingly, (Fig. 1 (b-d)) illustrates various steps/phases involved in the AFSD. Firstly, the revolving tool head assembly is lowered towards the substrate so that a minimal gap persists between tool and substrate with the help of tool protrusions (Fig. 1 (b)). After that, the rotating feed rod is translated downwards through the tool cavity with a low feed rate to achieve contact between substrate and feed rod. Once contact is made, the rotating feed rod generates frictional heating under given actuator force and tool torque, raising its temperature (Fig. 1 (c)). With time, the thermal softening effect becomes prominent, and the downward thrust of the feed rod initiates material deformation at the feed rod- substrate interface. Following the above, the deformed material gets extruded between the tool-substrate gap (Fig. 1 (d)). Finally, the tool head assembly is linearly traversed along the substrate in which the deformed material undergo extrusion, stirring, shearing, and deposition (Fig. 1 (a)). Once the concerned layer is deposited, the tool head assembly is raised per desired layer thickness, and the above process is repeated during subsequent layer by layer deposition.

It is worth noting that, based on prior experiments [25] the optimum material feed rate was maintained at 50 % of the tool linear velocity to get a successful deposit with minimal flash, henceforth in the manuscript this condition will be referred to as optimum feeding condition. Experimental parameters are listed in Table 1. Onboard sensors were utilized to collect temporal variation in process attributes such as actuator force and tool torque. In order to calculate the energy input with varying process parameters, specific linear energy density (E_s) which relates to tool rotational speed (ω) and tool linear travel speed (V) and tool torque (M) is defined as follow
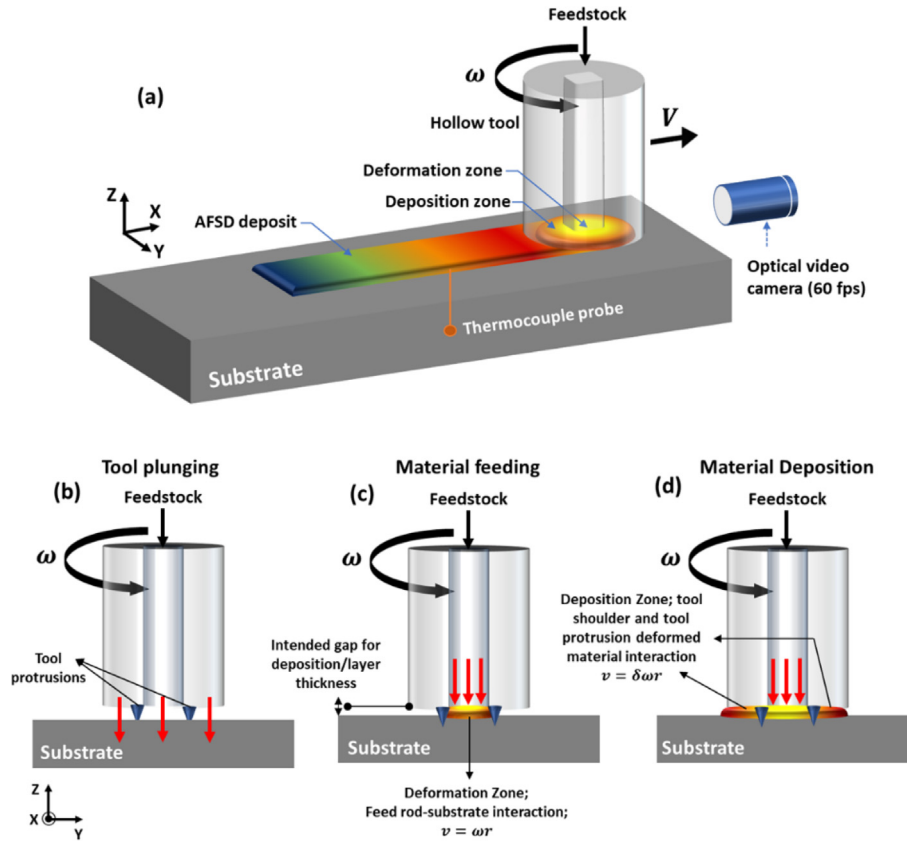
Fig. 1. Schematic representation of (a) MELD experimental setup for additive friction stir deposition (AFSD) of AZ31B Mg, and sequential steps involved in the deposition process (b) tool plunging, (c) material feeding and (d) material deposition. (Note that for the sake of visual aid, the tool protrusions are not illustrated in Fig. 1 (a), rather they are represented in the cross-sectional view with accurate spatial location).

Table 1
List of experimental parameters and evaluated specific energies during AFSD of AZ31B alloy.

Tool rotational speed ω	Tool linear travel speed V	Tool Torque M	Specific Energy
400 rpm	4.2 mm/s	132 Nm	210 J/mm
400 rpm	6.3 mm/s	143 Nm	151 J/mm

$$E_s \approx M \frac{\omega}{V} \qquad (1)$$

A type K thermocouple was embedded 4 mm beneath the surface of base plate directly below the center of the deposit to collect variation in temperature at that particular location while multiple layers were deposited (Fig. 1 (a)). Omega multichannel digital data acquisition module was utilized for recording the thermocouple data. The transient temperature recordings were collected at a temporal resolution of 1 s. The thermocouple data was utilized to validate the computational model. Several trials were carried out to find a successful materials processing window for the AFSD of AZ31B Mg. Previous publication by the authors provides detailed description of the AFSD process of AZ31B and multi scale observations of the deposits [25]. In addition, as the material is deposited in the gap between the tool and the substrate, the deformed material flow behavior in the above gap was examined in-situ with the help of an optical camera (60 frame rates per second go-pro camera) (Fig. 1 (a)).

Microstructure evolution in AFSD AZ31B was characterized with the aid of electron back scatter diffraction (EBSD). Thermo Fisher Nova Nano SEM 230 scanning electron microscope (SEM)

equipped with Hikari super detector operated at 20 KeV was used for acquiring EBSD scans. Sample preparation for EBSD consisted of a two-step approach of mechanical and ion polishing. First the samples were mechanically polished using 800–1200 grit SiC papers with ethanol as the lubricant. Mechanical polishing was then continued on Buehler texmet cloths with diamond suspensions of 1 and 0.25 μm average particle sizes respectively in ethanol medium. Final stage included mechanical polishing using 0.06 μm silica suspension on a Buehler chemomet cloth. The mechanically prepared samples were then cleaned using ethanol and immediately transferred to Gatan 682 ion polishing system operated at 5 KeV voltage and 190 μA current for the next step in sample preparation. The sample was kept at 4° angle with respect to the ion gun and polished for 30 s to obtain a mirror finish suitable for carrying out EBSD scans. The EBSD dataset was post processed on TSL OIM 8.0 software to extract orientation image maps (OIM) and Kernel average misorientation (KAM) maps. A Thermo-Fisher Nova 200 Nanolab dual beam focused ion beam (FIB) microscope was used for the preparation of cross-sectional transmission electron microscopy (TEM) foils. TEM imaging was performed using a Thermo-Fisher Tecnai G2 F20 microscope operating at 200 kV to obtain micrographs and corresponding selected area diffraction patterns (SADP).

2.2. Numerical modeling

In order to predict accurate thermal evolution during AFSD, consideration of frictional heating as well as heat generation due to plastic deformation is necessary. As discussed above, the AFSD process can be categorized into two spatial regions. The material

directly underneath the feed rod predominantly experiences frictional heating at the feed rod/substrate interface followed by its deformation due to thermal softening. Thus, the region beneath the feed rod can be termed as "deformation zone" (Fig. 1(c-d)). Thereafter the deformed material gets extruded between the tool substrate gap, and depending upon conditions such as temperature, friction, and material properties; the deformed material either fully slips or partially sticks/slips under the moving tool shoulder. This region can be termed as "deposition zone" (Fig. 1 (d)). The slipping behavior under the tool shoulder varies with the deposit material. For instance, Cu-AFSD deposition has been observed to occur with fully slip conditions beneath the tool shoulder. Whereas Al6061-AFSD showcased partial stick/slip behavior [26].

In light of the above-described physical process occurring during AFSD, prior to mathematical formulation in the deformation and deposition zones it is essential to evaluate the nature of slipping experienced by the material during AFSD. To this end, preliminary observations were conducted using an optical camera setup (60 frame rates per second go-pro camera) to understand flow behavior of AZ31B alloy under AFSD conditions. Fig. 2 provides still-frame images from the in-situ optical camera, in which the revolving tool, deformed material underneath and substrate are annotated for reader's reference. In addition, for more clear visualization of the flow behavior, the in-situ videography of the same image has been provided as a supplementary material (refer to the online version of the article). In order to assess the state of material flow in the deposition zone (material underneath tool shoulder), a material point is marked (Fig. 2 (b), marked point "A") and the change in its relative position is observed for the duration of next six seconds (Fig. 2 (c)). The marked point "A" is observed to have travelled a distance of 10.6 mm relative to its original position. Thus, the linear velocity of the marked point "A" in the observed images is ~ 1.76 mm/s which is roughly 1 % of tool rotational velocity at the same radius. Therefore, under such conditions and as confirmed through the in-situ photographic observations (Fig. 2), the material flow under the tool shoulder was dominated by slip mechanism. Also, the in-situ photographic observations indicated that the deformed material under the tool shoulder appeared to translate radially away from the tool center rather than moving along the rotating tool shoulder. Therefore, in case of AZ31B alloy, deformation zone is characterized as per sticking condition [22], where the frictional heating and plastic deformation occur. The deposition zone entails material slipping with frictional heating due to the rotating tool shoulder.

In AFSD, previous studies have reported optimum deposition conditions as 50 % ratio of travel speed and actuator feed rate. When this ratio is<50 %, so called starved deposition condition is observed, with apparent gaps and truncated build profile. Whereas ratio higher than 50 % results in overfed deposition with excessive flash and wider build profile. However, the effect of feeding condition on temperature is minimal [15,26]. Therefore, in the context of developed model within the framework of process thermokinetic-structure linkage, optimum feeding conditions have been assumed to be in effect.

Other than frictional heating, plastic deformation and material sticking/slipping behavior in the deformation and deposition zone, the deformed material interaction with the tool protrusion might have possible bearing on the AFSD deposit. Geometrically, the tool protrusion height is roughly 1.5 mm, thus for a layer thickness of 1 mm, the tool protrusion will interact with both substrate/preceding layer and the layer being deformed/deposit. However, the surface area of these protrusions is significantly less than that of the tool assembly (ratio of 1:100). Thus, on a global scale the presence of protrusion will have minimal effect on heat generation and material flow mechanism. Therefore, for the sake of simplicity in

thermal model formulation effects related to tool protrusion has been neglected in this study. Note that, during the deposition of AZ31B Mg any noticeable effect of tool protrusion on microstructure morphology has not been observed in the present study (discussed in subsequent sections).

Under the premise of above discussion, a 3D pure conduction based thermal formulation of multi-layer AFSD is developed. Further, to account for plastic dissipation in the deformation zone, a pseudo-mechanical formulation based on the theory of FS and CDFW is proposed [27–31]. Accordingly, the following assumptions are considered in the proposed computational model: -.

1. The model assumed a steady-state deposition under optimum feeding conditions as the basis of the thermal formulation.
2. Thermal contribution of dwelling stage during deposition is considered insignificant.
3. The effect of tool protrusions on temperature evolution was disregarded. As the protrusion surface area is much smaller than that of tool surface, and the interfacial heat generation at protrusion substrate/deposit interface is expected to be small [26].
4. The volumetric heat generation owing to plastic dissipation was assumed to restrict in the deformation zone. Further, the deformed material was considered to stick at the feed rod/substrate interface during plastic deformation.
5. Since the linear velocity of the tool (4.2 mm/s and 6.3 mm/s) is significantly lower than the rotational velocity (400 rpm, equivalent to ~ 798 mm/s maximum linear speed for the tool of outer diameter of 38.1 mm), it is assumed that the material flow is predominantly governed by the rotational motion than the linear motion of the tool. Hence, the material flow velocity in the deformation zone was assumed to be centro-symmetric with torsion like state. In view of this, the variation in its magnitude considered to occur radially depending upon tool rotational speed.
6. A plasticized feed material layer thickness was defined as the region, where the material velocity decayed exponentially from its maximum at elastic–plastic feed rod interface towards fully sticking feed rod/substrate interface.
7. Temperature evolution and associated stress and strain rate due to plastic dissipation in the deformation zone is based on the centro-symmetric material velocity formulation.
8. The material properties were treated as isotropic, homogenous, and temperature dependent.

2.2.1. Governing equation

The governing equation pertaining to conduction-based heat transfer can be expressed as follows: -

$$\rho C_p \frac{\partial T}{\partial t} + \rho C_p \left(\overrightarrow{u} \cdot \nabla T \right) = \nabla \cdot (k \nabla T) + Q'''_{plastic} \tag{2}$$

Importantly, the term $Q'''_{plastic}$ represents the volumetric heat generation. In context of AFSD $Q'''_{plastic}$ can be related to the volumetric heat generation due to plastic dissipation, and its formulation is discussed in subsequent subsection.

2.2.2. Frictional boundary conditions

As discussed in the sections above, friction heating occurs at the feed rod/substrate interface in the deformation zone and tool shoulder/deformed material interface in the deposition zone. Therefore, based on the theory of pure conduction models on FSW [6,8], a surface heat flux boundary condition was employed to accommodate frictional heating during AFSD. The radially dependent boundary heat flux due to frictional contact between feed rod/substrate interface can be expressed as:

$$q_f = \tau_{yield} \times (\omega r - V \sin\theta); 0 < r \leq r_d \tag{3}$$
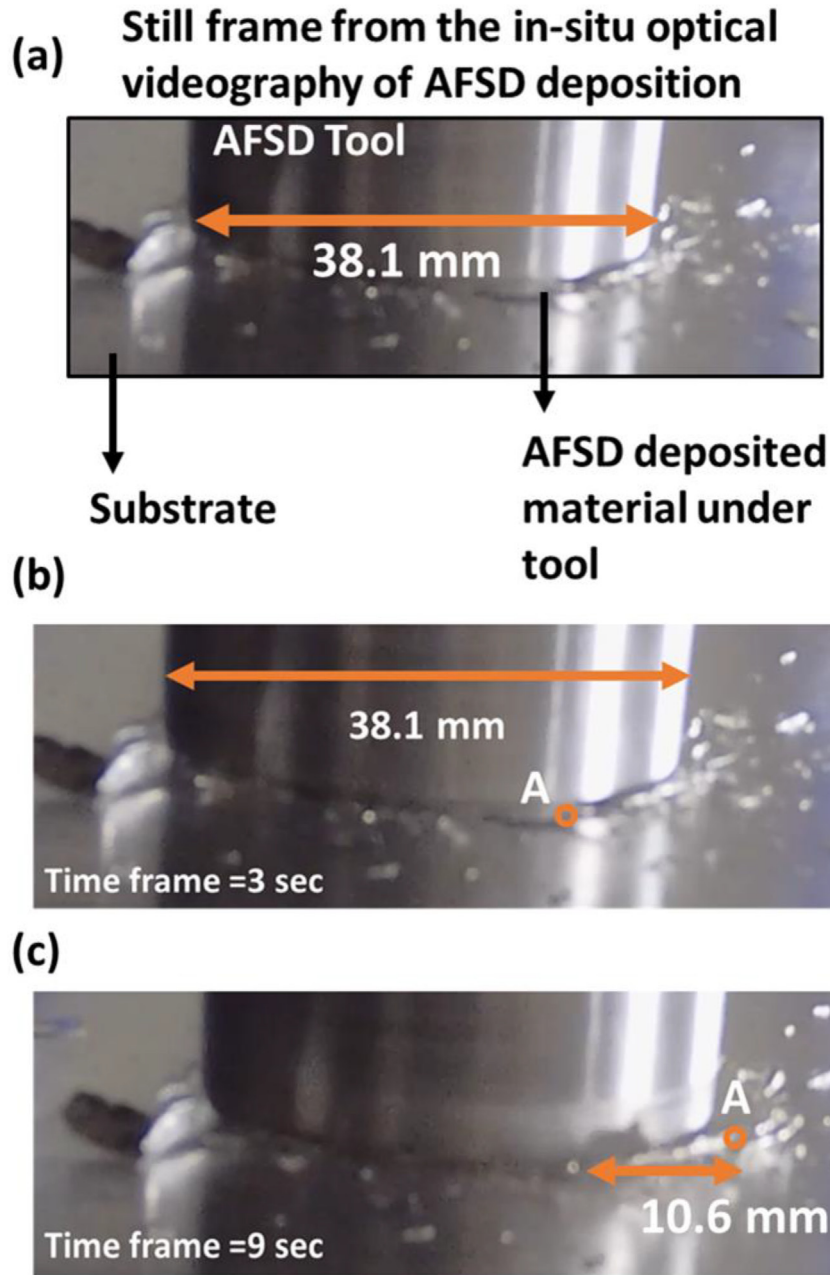
Fig. 2. The observed material flow behavior of AZ31B Mg under AFSD condition. tool rotational velocity 400 rpm and tool travel velocity 4.2 mm/s. (The in-situ videography of the material flow behaviour has been provided as a supplementary material, please refer to the online version of the article).

The underlying assumption of above formulation was on the basis of fully sticking contact condition under plastic deformation (Fig. 1 (d)). As the feeding material thermally softens and plasticizes, the shear stress τ_{yield} under sticking assumptions can be expressed as [32]

$$\tau_{yield} = \frac{\sigma_{yield}}{\sqrt{3}} \tag{4}$$

Note that the term σ_{yield} is temperature dependent. Similarly, the surface heat flux at extruded material/tool shoulder interface (Fig. 1 (d)) can be expressed as following

$$q_s = \tau_{tool} \times \delta(\omega r - V\sin\theta); r_d < r \le r_s \tag{5}$$

In the above equation, δ corresponds to the slip-rate signifying the sliding/sticking contact state of the extruded material under tool shoulder. Thus, $\delta = 1$ corresponds to fully sticking regime and $\delta = 0$ denotes fully sliding regime. In case of sliding/sticking regime, the value of δ ranges anywhere from 0 to 1. The term τ_{tool} is derived from back calculation using experimentally obtained tool torque (M) data during deposition [25], as explained below

$$M = \int_0^{2\pi} \int_{r_d}^{r_s} \eta \times r \times (\tau_{tool} r dr d\theta) \tag{6}$$

Furthermore, the slip rate [33] can be expressed as

$$\delta = 1 - \left(1 - exp\left(\frac{-\delta_o \omega(r - r_d)}{\omega_o(r_s - r_d)}\right)\right) \tag{7}$$

Where, δ_o is a scaling constant (<1) and ω_o is the reference value for the rotational tool speed. According to experimental observations, these values are adjusted to represent material flowability under the tool shoulder. For instance, for a given material that is readily extruded, covering a large portion of the tool shoulder area, the δ should gradually shift from 1 towards zero as r changes from r_d to r_s and vice versa. As discussed in the sections above, AZ31B exhibits dominating slip behavior under the tool shoulder, hence appropriate adjustments in the scaling constants (as shown in Fig. 3) were done to mimic the observed flow behavior. Thus, the above two position-dependent boundary heat flux conditions constitute the thermal contribution in the developed model.

2.2.3. Convection and radiation boundary conditions

All the boundaries associated with deposited material were assigned convective and radiative boundary conditions with respect to heat flow, as expressed below: -

$$q_{loss} = h_\infty (T_\infty - T) + \varepsilon \sigma (T_\infty^4 - T^4) \tag{8}$$

2.2.4. Pseudo-mechanical formulation in deformation zone

The general expression for volumetric heat generation due to plastic dissipation in the deformation zone can be expressed as

$$Q_{plastic}''' = \eta_{th} \sigma_e \dot{\varepsilon} \tag{9}$$

In case of high-temperature and high strain-rate applications, **Sellars-Tegart** constitutive model is often used to describe the relation between effective stress and effective strain rate with the help of temperature compensated strain rate parameter Zener-Holloman parameter [9–11]. The corresponding equations are described below.

$$\sigma_e = \sigma_r \sinh^{-1} \left(\frac{Ze}{\alpha} \right)^{\frac{1}{m}} \tag{10}$$

In the above expression the terms σ_r, α, and m are calibration constants, whose values are taken from hot deformation calibration of AZ31B, listed in Table 2 [34]. The term Ze can be expressed as

Fig. 3. Variation of the slip rate (δ) with respect to variation in scaling constants. Deformation zone corresponds to the area under feed rod, whereas deposition zone is the area under tool shoulder. Note that term δ is meaningful in the deposition zone.

$$Ze = \dot{\varepsilon} exp \left(\frac{Q_{act}}{RT} \right) \tag{11}$$

The value of activation energy Q_{act} is taken as 151 kJ/mol as per high strain rates problems. Note that the deformation mechanism in AZ31 alloy changes with process conditions and thus a change in material constitutive behavior (and material constant Q) is expected. In case of AFSD the expected strain rates and temperature is very high [25]. Accordingly, the value of apparent activation energy in case of high strain rate as well as high temperature reported during hot deformation case study has been adopted [35]. Note that there is a slight variation in reported Q values in the high strain rate and high temperature regime [36–38], a sensitivity analysis was employed and the best suited value of Q yielding acceptable T evolution was selected. That is 151 kJ/mol as reported in [35,37].

Lastly, on the basis of centro-symmetric strain rate assumption on FS and RFW problems [27,30,31] the equivalent strain rate in the deformation zone can be expressed as

$$\dot{\varepsilon} = \delta_\varepsilon' \frac{\omega R_l}{\delta_{pl}} \left(\frac{1}{\delta_\varepsilon} exp \left(\frac{z - z_i}{\delta_{pl}} \right) \right), R_l \leq r_d \tag{12}$$

$R_l(x, t)$ moves along the deposited area as per tool traverse speed, δ_ε and δ_ε' prescribe the upper limits of the deformation zone radially. The term δ_{pl} scales the variation of strain rate along the z-direction in the deformation zone. The experimental evaluation of δ_{pl} is difficult, however its upper limit can be the prescribed layer thickness. In addition, the extent of plastic deformation primarily depends on tool rotational and traverse speeds. Thus, as a first level of approximation, the plasticized layer thickness is expressed in the following manner [39], where δ_{pl}' is a scaling constant.

$$\delta_{pl} \cong \delta_{pl}' \frac{V}{\omega} \tag{13}$$

2.2.5. Numerical solution procedure

Fig. 4 illustrates the schematic representation of the longitudinal cross-section of the computational domain. A quiet element activation/de-activation strategy was employed to incorporate the multilayer deposition [40,41]. For any given point during deposition, the material preceding the moving tool area corresponded to deposited material. Hence, the material properties of the consolidated material have been assigned to those elements. For the rest of the elements, material properties of air were assigned. In other words, the activation or de-activation status of mesh elements depends upon the transient tool position for each layer.

The above formulation completes the multilayer frictional heating thermal model for AFSD. Note that all the thermophysical parameters discussed above are temperature dependent and are listed in Table 2. Note that in the developed model, the variation of tool torque (M) due to change in ω or V is incorporated in the frictional boundary condition (Eq. (5)), in which direct input from experiments are utilized. Moreover, stick/slip behavior of the deformed material in the deposition zone is included on an ad-hoc basis (based on experimental observations) with the help of slip rate coefficient δ.

In sum, the developed model incorporates pertinent process parameters such as (M, ω, V) on a physics-based premise. Whereas parameters such as (δ_ε, δ_{pl}, δ_o, ω_o) are included on an ad-hoc basis which are meaningful in a limited process window (such as optimum feeding condition). Moreover, the choice of values of (δ_ε, δ_{pl}, δ_o, ω_o) are not arbitraray, rather it depends upon material deformation characteristics, as stated earlier were observed through in-situ photographic recording of the AFSD process. The above mathematical model was executed on a commercial FEA software COMSOL Multiphysics®. The solution algorithm is defined
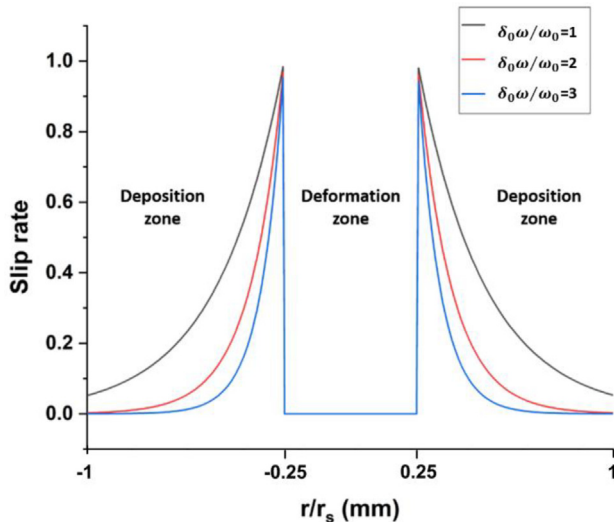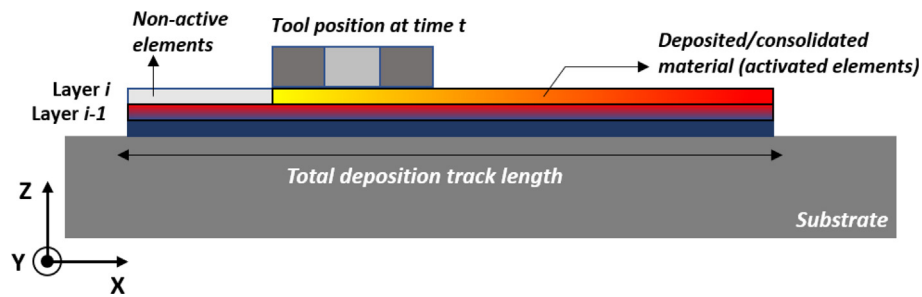
Table 2

List of thermophysical parameter and material constant employed in the numerical model.

Thermophysical Properties of AZ31 [42]				Density
Thermal Conductivity		Specific Heat		
T [°C]	$k[W/mK]$	T [°C]	$C_p[J/kgK]$	$\rho[kg/m^3]$
20	76.9	20	1040	1780
50	83.9	100	1042	
100	87.3	300	1148	
150	92.4	>600	1414	
200	97			
250	101.8			
424	118.5			
630	60			
635	120			
680	240			
Material Constants [25,34]				
$\sigma_{yield}[MPa]$	$1.067 \times 10^{-3} \times T^2 - 1.969 \times T + 898.056$			
$h_\infty[m^2K]$	$\begin{Bmatrix} 35, r \leq r_d \\ 20, r_d < r \leq r_s \\ 10, elsewhere \end{Bmatrix}$			
T[°C]	25			
$\sigma[W/m^2K^4]$	5.67×10^{-8}			
ε	0.5			
$\sigma_r[MPa]$	53.3			
m	1/4.36			
$\alpha[1/s]$	7.78×10^8			

Fig. 4. Schematic representation of layer activation strategy adopted during thermal model of multilayer AFSD.

in Fig. 5, in which the ad-hoc parameters were adjusted iteratively to achieve conformity with experimental results. An adaptive meshing strategy (dependent upon temperature and thermal gradient of mesh elements) was employed to achieve reasonable computational time considering the pure conduction problem. The dimension of each deposited track is 100 × 38 × 1 mm³. Accordingly, the adaptive meshing strategy ensures a minimum element size of 0.5 mm in the instantaneous region directly beneath the moving tool. The choice of 0.5 mm element size was based on mesh sensitivity analysis. The computational run time for consecutive 5-layer deposition was<20 min on an Intel(R) Xeon (R) (Gold 6252 CPU @2.10 GHz-190 GB) processor.

2.2.6. Experimental validation

The validation of the proposed thermal model was assessed using thermocouple temperature measurements. A K-type thermocouple was inserted 4 mm below the substrate surface at the center location of the deposition. Fig. 6 depicts the comparison of thermocouple and simulated thermokinetic evolution at the exact location for $E_s = 210J/mm$. The temperature peaks in Fig. 6 are associated with each track's deposition during AFSD. As can be observed, the thermal model provides reasonable agreement with the actual thermal evolution during the AFSD as it captures the essential thermal events in the region of interest. The minor variations from the actual temperature profile (Fig. 6) can be attributed to difference in the size of actual base plate used in experiments to

that of computational domain size. Note that there is slight temperature drop across different layers, this marginal error is associated with the re-initialization of the problem once the new layer activates. Overall, the effect of such discontinuity in change in layer has minimal effects on the thermal representation of the model. In addition, Table 3 provides comparison between peak temperature data obtained from multi-layer experiments for both the process conditions, the error is within 9 %. It is remarked that despite the limitations of the developed model in terms of its incorporation of ad-hoc parameters (δ_ε, δ_{pl}, δ_o, ω_o), the model predicts temperature evolution and thermal cycle with acceptable agreement with experiments. More importantly, the present model establishes a framework for multi-layer thermo-mechanical predictions of AFSD process in a computationally efficient manner. In the sections below, the process-microstructure linkage has been elucidated based on the results of the validated pseudo-thermo-mechanical model for AFSD.

3. Results and discussions

3.1. Thermal evolution during AFSD

As discussed in the sections above, heat generation during AFSD is primarily associated with 1) frictional contact heating at the feed rod/substrate interface and deposit/tool (tool shoulder) interface, and 2) plastic dissipation at the feed rod/substrate region (defor-
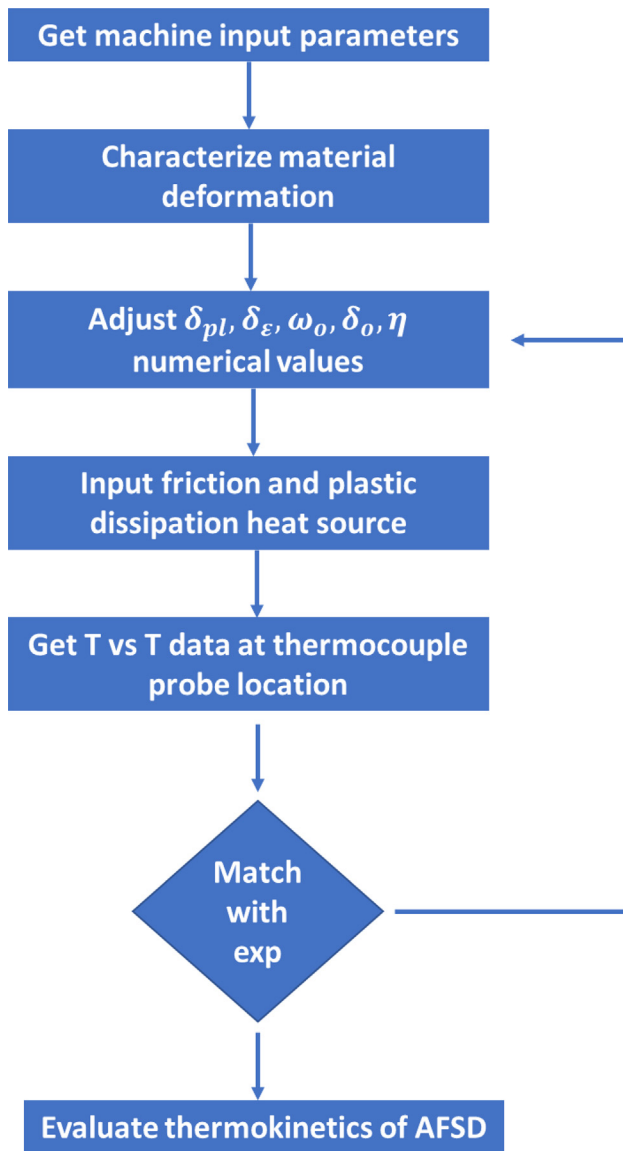
Fig. 5. Computational strategy adopted in thermal modelling of multilayer AFSD.

Fig. 6. Comparison of thermal profiles obtained from simulation (red lines) and experiments (black lines) for a 5-layer AFSD deposition ($E_s = 210 J/mm$). Note that thermocouple probe was embedded 4 mm beneath the surface of substrate. (For interpretation of the references to color in this figure legend, the reader is referred to the web version of this article.)

mation zone). Therefore, it is essential to understand the thermal contribution of both of these physical phenomena during AFSD. Fig. 7 (a) and (b) present the top view and longitudinal cross-section (in the tool traverse direction) of temperature contours respectively during AFSD when both plastic dissipation and frictional heating are considered and the process parameter corresponds to $E_s = 151 J/mm$. As can be observed, the peak temperature is $600°C$ (Fig. 7), is very close to the melting point of AZ31Bb alloy $\left(T_s = 605°C, T_l = 632°C\right)$. Note that previous experimental measurements [4,15,26] on AFSD stir zone temperature have been reported in the range of $(50 - 93\% of T_{melt})$. Moreover, simulation studies reported stir zone temperature of AFSD exceeding its melting temperature (material: AA6061) [4,15,26]. In addition, peak temperatures in RFW/FS have also been reported to attain maxima near melting temperatures [43,44].

Furthermore, the maximum temperature region during AFSD is in the vicinity of the deformation zone (Fig. 7 (b)). There is a slight drop in the temperature field inside the deformation zone, which can be attributed to centro-symmetric strain approximation (As the strain rate formulation largely varies with the tool rotational
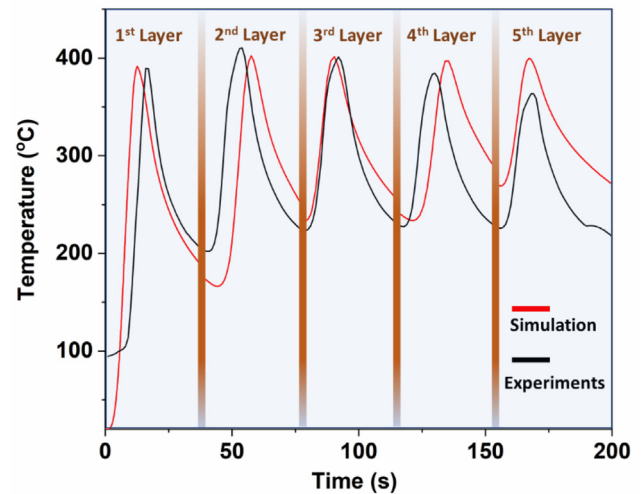
speed, the ωR_l term in eq. (12) will increase with the radial direction, hence the contribution of $Q'''_{plastic}$ will be less towards the center of the deformation zone.) and conduction losses to the undeformed feed rod.

Another important observation is contour profiles corresponding to T $380°C$ extended up to 4 mm depth into the substrate. This observation has been validated with the thermocouple measurement presented in Fig. 6. In addition, the overall thermal profile inside the tool area ($R \leq r_s$) is uniformly distributed with a slight drop in the temperature at the leading edge of the tool. This can be reasonably explained with the help of the slip factor (δ). As discussed in section 2.2.2, the deformed AZ31B material covers the region beneath the tool shoulder under a slip dominating contact state that was also confirmed from the in-situ video recording of the AFSD process. Therefore, although the term $(r\omega)$ increases, the term $((1 - \delta) \times r\omega)$ decreases as r moves from (r_d to r_s), hence the frictional heat contribution term in Eq. (4) decreases resulting in the drop in the temperature profiles.

More importantly, the present results indicate symmetric temperature distribution on both the advancing and retreating sides of the moving tool. This aspect has been discussed in a previously reported AFSD model with optimum levels of actuator feed rate [15]. This observation is contrary to asymmetric temperature distribution in the FSW process as the marginal temperature difference in advancing and retreating sides is observed (Fig. 7 (b)). The primary reason for this aberration is the majority of heat generation in the deformation zone is due to plastic dissipation and feed rod/substrate interaction in AFSD. Whereas, in the FSW, tool shoulder material interaction results in frictional and plastic dissipation. Another distinction from FSW is the partial/entirely slipping behavior of the deformed material underneath the tool shoulder during AFSD. Nevertheless, the present model assumes the case of optimum actuator feed rate to ensure uniform deposition and minimal aberration in the temperature in advancing and retreating sides of the tool.

Finally, during any point in the deposition interval, the deformed material AZ31B will experience temperature in the range of $\left(400 - 600°C\right)$ while traveling from the deformation zone to the deposition zone. The duration of the above thermal exposure pri-

Table 3
Evaluation of numerical model on the basis of peak temperatures obtained from AFSD multilayer experiment.

Layer No.	$E_s = 210J/mm$			$E_s = 151J/mm$		
Thermal evolution in AFSD	Simulation (°C)	Experimental (°C)	% error	Simulation (°C)	Experimental (°C)	% error
1st layer	391.92	389.28	0.51	381.7	373.59	2.17
2nd layer	402.18	411.17	2.1	388.05	406.85	4.62
3rd layer	401.76	400.49	0.3	389.8	407.51	4.34
4th layer	397.03	384.20	3.38	381.2	397.36	4.06
5th layer	399.54	364.42	9.64	381.6	390.88	2.35
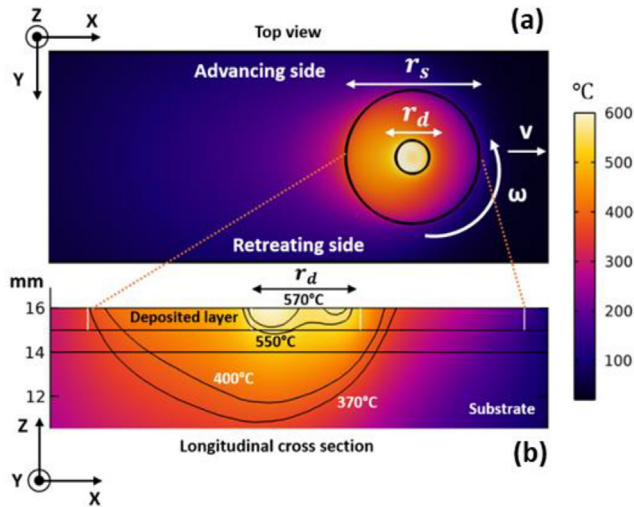
Fig. 7. Simulated thermal evolution during AFSD with consideration of frictional heating and plastic deformation. (For interpretation of the references to color in this figure legend, the reader is referred to the web version of this article.)


Fig. 8. Simulated thermal evolution during AFSD with consideration of only frictional heating. (For interpretation of the references to color in this figure legend, the reader is referred to the web version of this article.)

marily depends on the tool linear travel speed (V). Naturally, for a given rotational speed of the tool (ω), variation in V will result in different exposure durations. Hence, any change in thermal exposure time duration (as a consequence of varying V) will affect the final microstructure of the deposited material. The significance of the extent and duration of thermal exposure of material during AFSD to microstructural evolution is discussed later in the following sections.

In order to probe the role of plastic deformation in dictating the thermal evolution, simulations were run with only consideration of frictional heating and resulting temperature distribution is presented in Fig. 8. A significant reduction in peak temperature from 600 to $400°C$ can be noticed. Further, the overall temperature profile around the tool (advancing and retreating side) is significantly more asymmetric with a higher temperature region on the retreating side of moving tool/feed rod assembly. Finally, the temperature contour profile corresponding to $T = 300°C$ is observed in the region 4 mm below substrate, which is a substantial underestimation (of around $\left(100°C\right)$) compared to the case described above and the experimental thermocouple data (Fig. 6). This demonstrates the importance of the consideration of heat generation due to plastic deformation (in the deformation zone) for accurate estimation of the thermokinetic evolution during AFSD.

3.2. Thermo-mechanical evaluation of deformed zone

Based on the pseudo-mechanical formulation described in the earlier sections, temperature, strain rates, and flow stress in the deformation zone are appraised for both the sets of processing parameters (Table 1), with the help of the transverse cross profiles
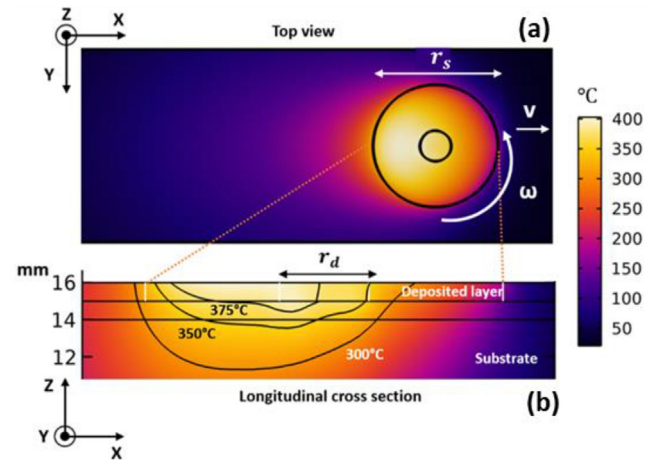
shown in Fig. 9. As can be observed, higher magnitude of temperatures and strain rates are observed in case of $E_s = 210J/mm$ as compared to that of $E_s = 151J/mm$. In contrast, the stress contour profiles have larger spread of high magnitude stress (120 MPa) in case of $E_s = 151J/mm$.

The higher temperature in $E_s = 210J/mm$ can be related to the relatively slower linear tool travel speed of 4.2 mm/s (Table 1). For a given rotational speed, when the tool linear travel speed increases the thermal exposure time decreases, as a result thermal effects are less pronounced. In addition, the formulation of $\dot{\varepsilon}$ (strain rate), Ze (Zener-Holloman parameter), and σ (Flow stress) and in turn $Q'''_{plastic}$ (volumetric heat generation due to plastic deformation) depend on ω (tool rotational speed) and δ_{pl} (plasticized layer thickness beneath feed rod) (Eqs. 8–12). In case of $E_s = 210J/mm$, $\delta_{pl} \approx 650\mu m$, which increases up to $\delta_{pl} \approx 1000\mu m$ for $E_s = 151J/mm$. Therefore, small plasticized layer thickness in $E_s = 210J/mm$ facilitate larger strain rates contributing towards higher $Q'''_{plastic}$ resulting in development of higher temperatures.

Furthermore, generation of higher strain rates in $E_s = 210J/mm$ are observed Fig. 9 (c) and (d). As explained above strain rates during AFSD depend on relative velocity of the deformed material in the deformation zone. According to Eq. (11), the strain rate $\left(\dot{\varepsilon} \approx r\omega\frac{1}{\delta_{pl}}\right)$ is related to ω, V and $\delta_{pl} = V/\omega$. In both sets of the processing conditions (Table 1), ω is same, hence increase in V augments δ_{pl} and the magnitude of strain rate decreases. The physical significance of increased δ_{pl} is ineffective material deformation. As observed in Fig. 9 (c) and (d), increase in δ_{pl} corresponds to lower strain rate. It is worth noting that unusually high V will result in lower strain rates signifying ineffective material deformation, leading to process aberration such as gaps and voids in the deposit [25].This implies that at exceedingly high travel speed,
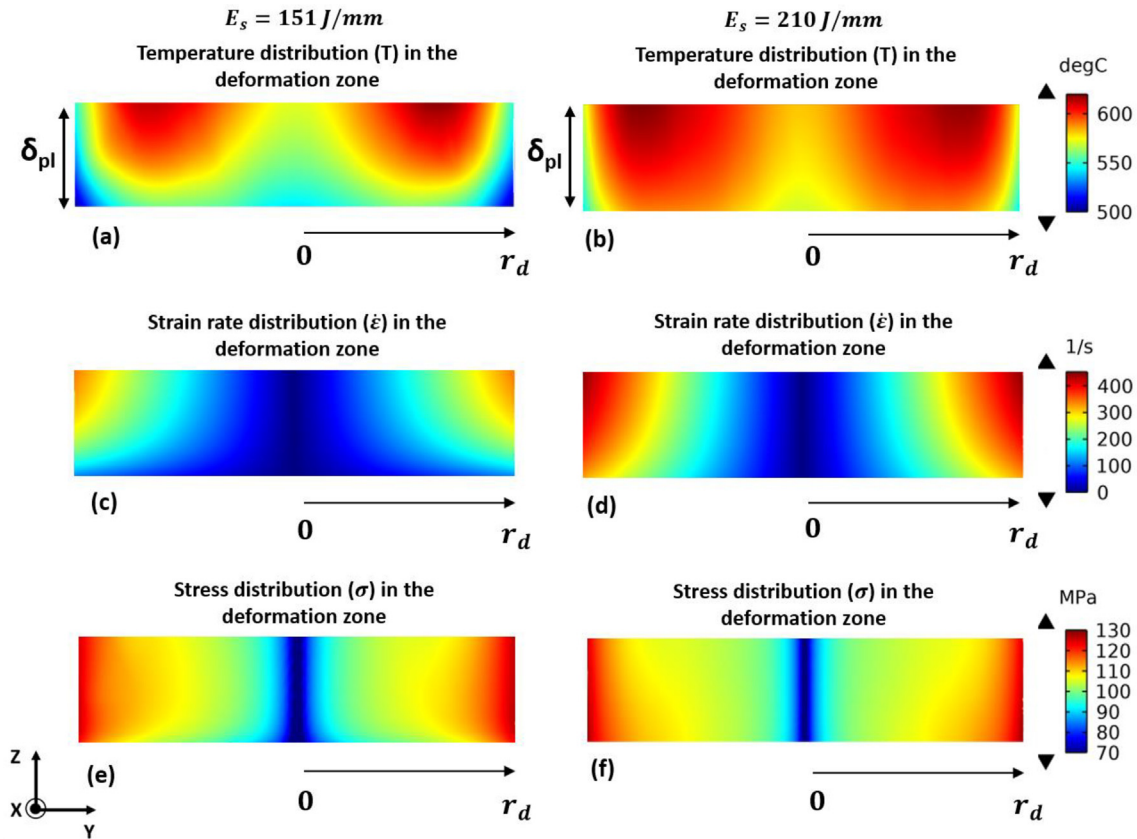
Fig. 9. Thermo-mechanical evaluation in the deformation zone, (a) and (b) Temperature contours, (c) and (d) strain rate contours and (e) and (f) stress contours. (For interpretation of the references to color in this figure legend, the reader is referred to the web version of this article.)

the term δ_{pl} will likely to become meaningless due to hindrance in material deformation. Therefore, in the developed model, formulation of δ_{pl} is applicable to a narrow process window where material deposition is possible.

The flow stress distribution inside the deformation zone for both sets of processing conditions (Table 1) has been presented in Fig. 9 (e) and 9 (f). In both cases, the maximum stress magnitude is around 130 MPa near the edge of the deformation zone. Since the higher temperature region is localized in the central deformation zone, the stress value attains its peak near the periphery of the deformation zone due to drop in temperature within this zone. Note that the material is not yet deposited ahead of the travelling tool assembly. Therefore, peak stresses observed near the boundary of the deformation zone can be considered as the stresses experienced by the substrate. Nevertheless, in-depth analysis using fully coupled thermo-mechanical models are required to understand the precise state of stress during AFSD, which is outside the scope of this work. Lastly, the spread of higher magnitude stress (>110 MPa) is extensive in $E_s = 151 J/mm$ compared to $E_s = 210 J/mm$ due to the development of lower temperatures in the deformation zone as discussed earlier.

In summary, the above results indicated the capabilities of the developed numerical model in predicting thermokinetic evolutions during the complex AFSD. Further, the proposed pseudo-mechanical formulation of the deformation zone provides important information of strain rate and temperatures which are extremely difficult and /or complex, if not impossible, to probe during AFSD process. The predicted thermo-mechanical parameters are essential in understanding the microstructure evolution, which is discussed in the subsequent section.

3.3. Evolution of microstructure and texture during AFSD

This section provides details on microstructural evolution during the AFSD process and its correlation with various AFSD process parameters (T, $\dot{\varepsilon}$, Ze and σ) derived using the numerical model developed in the present study. The EBSD inverse pole figure (IPF) maps of the AFSD deposits for both processing conditions and the feedstock have been presented in Fig. 10. These microstructures correspond to the longitudinal cross-section (XZ plane) located spatially at the central (bottom of third deposit layer) area of the AFSD deposits.

The feed stock material exhibits a relatively non-uniform microstructure with a wide grain size distribution (Fig. 10(a)). As stated earlier in section 2.1, the material data sheet provided by the supplier, the AZ31B Mg plate (from which the feed stock was machined) was produced via wrought processing followed by H24 tempering (170–200 °C). Although the temperature range of H24 heat treatment is not in the range of recrystallization temperature of AZ31B Mg, it appeared to have generated heterogenous microstructure along with multiple twins (Fig. 10). Further, the coarse grains appeared to possess significant intragrain misorientations as revealed by color gradients in the IPF maps. Several reports on post annealing examination of wrought processed AZ31 have observed similar microstructures [45–47]. Additionally, it can also be observed that the grains of the feed stock were distinctly non-equiaxed. On the contrary, microstructures of AFSD samples exhibited lower degree of microstructural heterogeneity with relatively higher grain size, lower intragrain misorientations, and more equiaxed grains. The two AFSD samples however, differed between themselves with respect to certain features.
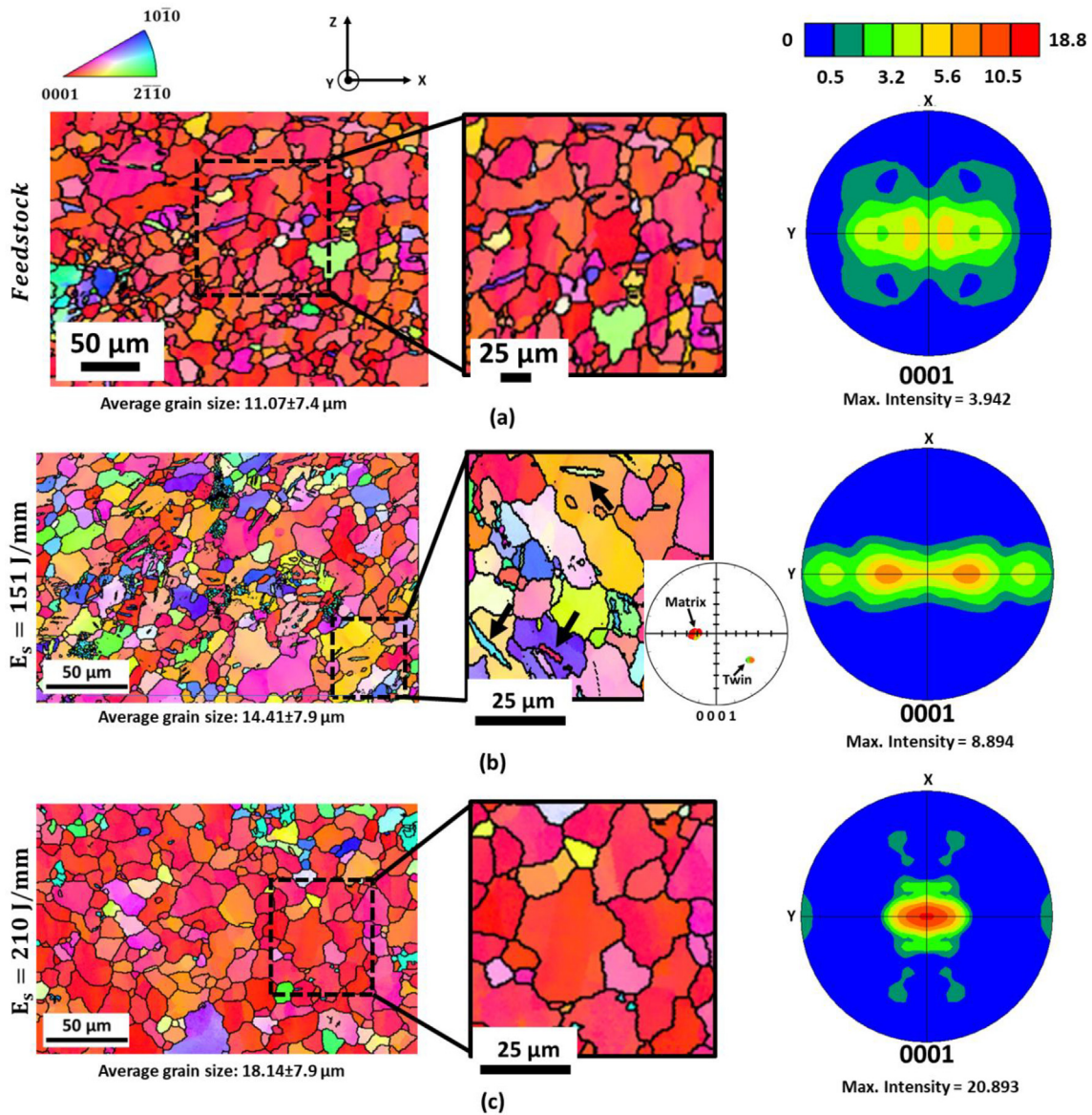
Fig. 10. The EBSD IPF micrographs and corresponding grain size distribution and crystallographic texture plots of (a) feedstock, (b) AFSD Es = 151 J/mm and (c) AFSD Es = 210 J/mm respectively. The pole figure plots were imposed with orthotropic sample symmetry. The features of interest (for example Twins, marked by black arrows) were shown as high magnification insets. The identification of twins was confirmed by their respective misorientation with parent, as shown in the pole figure.

$E_s = 210J/mm$ processing condition is characterized by the presence of coarser and more equiaxed grains (Fig. 10 (c)) in comparison to its $E_s = 151J/mm$ processed counterpart (Fig. 10 (b)). While the $E_s = 151J/mm$ processed sample contained noticeable fraction of deformation twins (which was identified to be $85°@$ $\begin{bmatrix} 2\bar{1}\,\bar{1}\,0 \end{bmatrix}$ tensile twins, Fig. 10 (b)), $E_s = 210J/mm$ processed sample was clearly devoid of any such deformation twins. These observations can be rationalized based on the thermo-mechanical deformation conditions experienced by the deposited material, which are explained below.

Fig. 11 provides grain boundary misorientation distributions and estimated geometrically necessary dislocations (GND) density maps super imposed with low angle grain boundaries (LAGBs) and high angle grain boundaries (HAGBs) for both the processing conditions along with corresponding maps for feedstock. As can be observed, the KAM maps show significant spread of local misorientation in some of the grains for the feedstock. Whereas, in the case of AFSD samples (151J/mm, 210J/mm), the local misorientation

spread is mainly restricted to LAGBs or subgrain boundary, signifying a decrease in dislocation content. EBSD analysis of the grain boundary distribution among the AFSD samples indicated the presence of a predominant fraction of HAGBs compared to LAGBs in both the deformation conditions. This establishes the operation of dynamic recrystallization (DRX) in both of the AFSD conditions employed in the current study. However, presence of noticeable fraction of deformation twins in 151J/mm along with non-equiaxed and finer grain size distribution indicate that the extent of DRX was lower in case of 151J/mm samples compared to the one processed at 210J/mm. Another interesting difference between these two samples is in the spatial distribution of intragrain misorientation quantified through KAM and GND distribution maps in Fig. 11.

The 151J/mm sample is associated prevalently with a relatively narrower distribution KAM value ($<2°$) (Fig. 11 (e)). In contrast, the 210J/mm sample exhibited wider KAM distribution due to local pockets of high KAM regions (Fig. 11 (h)). These observations in
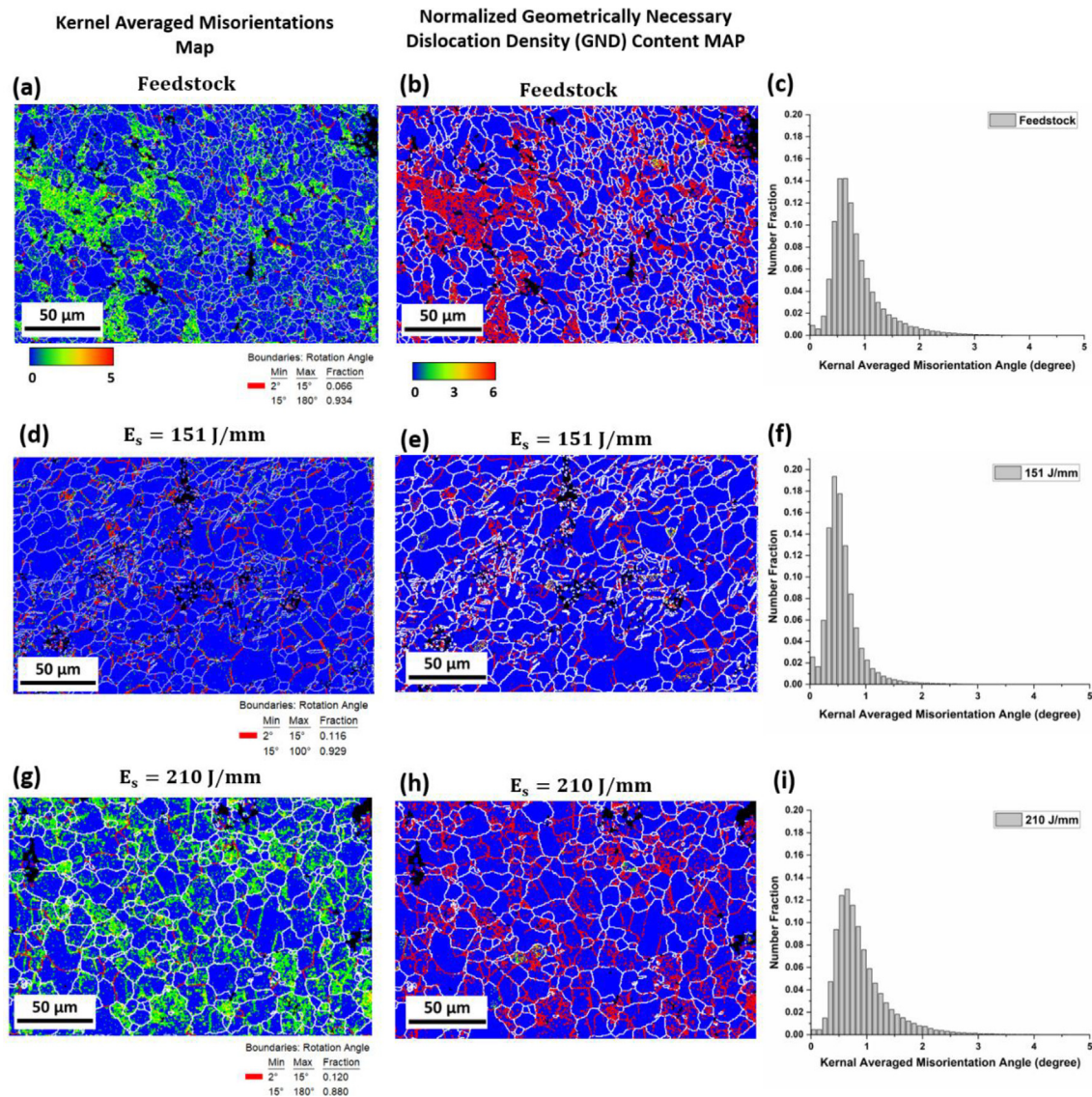
Fig. 11. KAM, normalized GND density maps, and KAM distribution comparison of feedstock ((a), (b) and (c)), AFSD $E_s = 151J/mm$ ((d), (e) and (f)), and AFSD $E_s = 210J/mm$ ((g), (h) and (i)).

conjunction with the results from numerical model (i.e., higher temperature and strain rate in 210J/mm case) suggested that extent of DRX was relatively high in 210J/mm sample. The KAM observations are consistent with the distribution of geometrically necessary dislocations (GND) in the microstructures (Fig. 11(b), 11(e), and 11(h)). The GND fractions of AFSD samples were normalized with respect to that in the feedstock.

The differences brought out by AFSD in the crystallographic texture distribution are also illustrated in Fig. 10. It is evident that the feed stock material had a relatively weaker texture with diffuse spread around the basal fiber ({0001}∥ND) (30 to 40°around transverse and tool travel direction). The spread in the basal texture considerably dropped in the 151 J/mm sample leading to classical transverse split in the basal poles. The 210 J/mm sample exhibited strong basal fiber parallel to ND axis. These observations can be attributed to the concomitant operation of deformation and dynamic recrystallization. In general, recrystallization is known to weaken the crystallographic texture through random nucleation of the new grains. However, the observation of progressively stronger basal texture from 151 J/mm sample (Fig. 10(b)) to 210 J/mm sample (Fig. 10 (c)) sample with higher DRX (210 J/mm) points

towards the possible operation of oriented growth being the primary mechanism [48] responsible for the observed sharpening of the resulting texture.

To further conduct preliminary microstructural observations in the feedstock and AFSD processed samples, TEM imaging was performed (Fig. 12). The bright field (BF) image of feed stock (Fig. 12 (a)) depicts a uniform distribution and high number density of $Mg_{17}Al_{12}$ precipitates along with dislocations within the grains (based on the observed dislocation contrast). On the contrary, the TEM micrographs of 151 J/mm AFSD deposit reveals a relatively reduced dislocation density and precipitate fraction. Recalling the thermal cycle presented in Fig. 6, and the thermal evolution discussed in Figs. 7 and 8, it is clear that material experiences repetitive heating and cooling cycles (of duration > 30 s) with temperature range of (200–600 °C). The above thermo-kinetic conditions conduce towards dissolution of the β-phase ($Mg_{17}Al_{12}$), more details about the dissolution of β-phase ($Mg_{17}Al_{12}$) during AFSD of AZ31B are discussed in detail in the recent publication by the current research group [49].

In summary, as observed from the TEM (Fig. 12) and EBSD analysis (Figs. 10-11), the high fraction of HAGBs and relatively low dis-
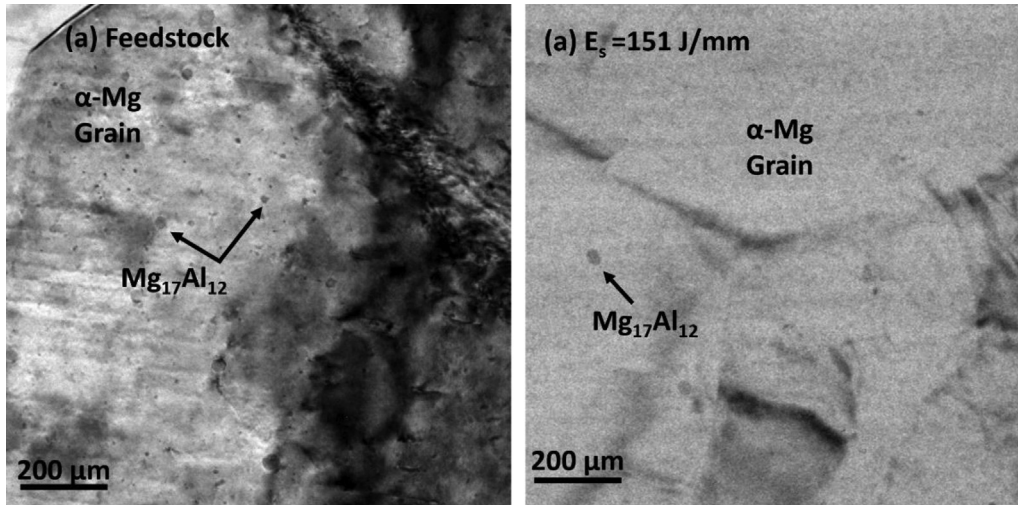
Fig. 12. Set of TEM data showing bright field (BF) images for (a) feedstock and (b) AFSD $E_s = 151 J/mm$.

location content for both the AFSD processing conditions further substantiate dynamic recrystallization (DRX) as the dominant mechanism during material deformation. Similar observation of DRX mechanism during hot deformation of AZ31Bb alloys, especially in high temperature regimes (>400 °C) with varying strain rates (0.001–100 1/s) have been reported in previous studies [24,50–56].

Fig. 13 provides comparison of microstructure morphology taken at different spatial regions of the transverse cross-section of the AFSD deposit. The selected spatial regions are the extreme ends and the center of the deposit. The extreme ends (marked as left and right region in Fig. 13) can be related to advancing and retreating side of the moving tool assembly. As can be observed from Fig. 13, for each of the experimental case (E_s = 210 J/mm, and E_s = 151 J/mm) there are no significant difference in the microstructural features amongst the different spatial regions in the AFSD deposit. Therefore, it can be inferred that the above represented spatial regions might have experienced similar (if not
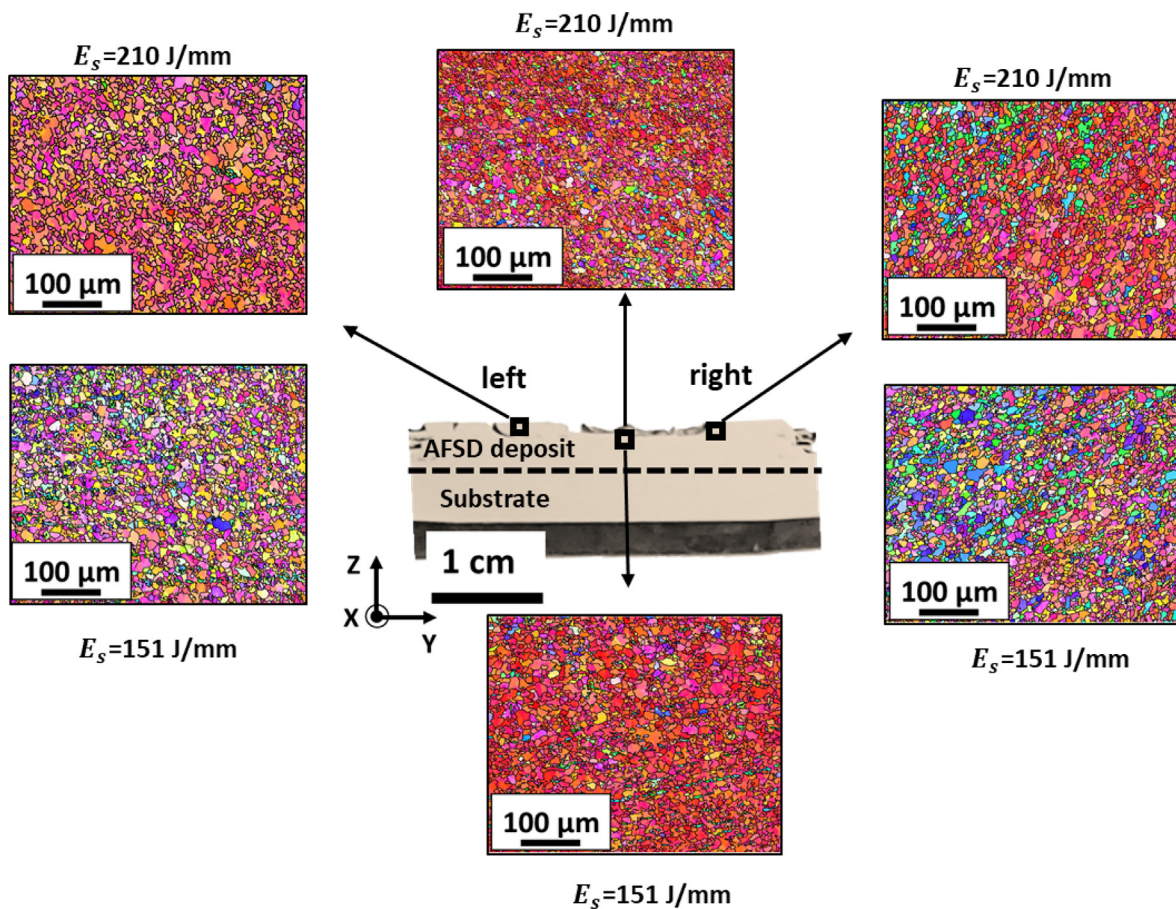

Fig. 13. Comparison of microstructure morphology obtained at different spatial locations of the AFSD deposit (transverse cross-section).

exactly the same) levels of temperature, stress and strain rates. The above observation also justifies that the centro-symmetric approximation of strain rate (discussed in section 2.2) employed in the current work.

3.3.1. Relating microstructure with Zener-Holloman parameter

In case of thermo-mechanical processing of metals, microstructural evolution is known to depend on severe plastic deformation and dynamic recrystallization, specifically at elevated temperatures [20,57–61]. The pertinent thermo-mechanical parameters are temperature, strain rate, and flow stress. The combined effect of above parameters on microstructural evolution during hot deformation is characterized using temperature compensated strain parameter known as Zener-Holloman (Ze) parameter (Eq. (10)). Accordingly, Ze distribution within AFSD deformation zone of AZ31B for both processing conditions and corresponding Ze process maps (variation of Ze as function of temperature and tool rotational speed) are presented in Fig. 14.

The general trend in thermo-mechanical processing is decrease in recrystallized grain size with increasing Ze parameter. This indicates that, lower temperature and higher strain rates leads to grain refinement. In earlier study on hot deformation (0.0001–1 1/s, 250–550 °C) of AZ31Bb alloy, the dependence of microstructural evolution with Ze have been elucidated [35]. The study reported initiation of DRX induced grain refinement for Ze > 10^{10}. In context of AFSD, naturally the strain rates are much higher than the case discussed above. However, high temperature (>350 °C) in the deformation zone compensates the extremely higher strain rates, resulting in Ze value in the range of 10^{11}-2×10^{12}, as shown in Fig. 14 (a) and 14 (b). Therefore, following the above rationale of high Ze (10^{11}-10^{12}) values, presence of DRX during AFSD can be rationalized. In addition, it is important to note that in case of temperature>400 °C, along with higher Ze values (10^{10}-10^{12}) substantial amount of grain growth consequent to DRX has also been reported in AZ31B [20,57–61]. Given the fact that Ze values depends upon strain rate (related to ω) as well as temperature, a process map of Ze (obtained using Eq. (10)) with variation in ω from 300 to 500 rpm (typical in AFSD) and temperature in 400–600 °C is presented in Fig. 14 (c). It can be observed that, in the high temperature regime the variation in ω (300–500 rpm), yields Ze values in the range of 10^{10}-7×10^{12}. Thus, in accordance with the above discussion, it is highly unlikely that microstructures in

AFSD will depict higher fraction of finer (DRX) recrystallized grains. This is further evident in the microstructural observations presented in Fig. 10.

Lastly, the presence of deformation twin can be related to the thermo-mechanical evolution in the deformation zone (Fig. 9). In plastic deformation of AZ31 alloys, deformation twins are often generated at the onset of deformation due to lack of slip-systems [62]. For instance, a hot compression test of AZ31 alloy reported generation of twins at early stages of deformation ($\varepsilon < 0.1$). Further, the study concluded that critical strain required for twinning is always less than for DRX in AZ31 alloys. Further, it has been reported that at higher temperature (>400 °C) the critical resolved shear stress required for activation of prismatic and pyramidal slip systems is less than that of twinning. Thus, it is plausible that under high strain rates (up to 400 1/s, as discussed in Fig. 9) during AFSD generation of twins might have occurred with the onset of deformation. As the AFSD progresses and temperature levels increased (>400 °C, Figs. 6-8) the deformation mechanisms might have shifted from twinning to other slip-based mechanisms. Following the above, another observation from Fig. 10 is lack/minimal presence of twins in case of $E_s = 210 J/mm$. Recalling the discussion on higher temperature, higher strain rates and longer thermal exposure duration (Note that total thermal duration in case of $E_s = 210 J/mm$ is close to 200 s where in case of $E_s = 151 J/mm$ the thermal duration is around 160 s) for $E_s = 210 J/mm$, it is highly likely that exposure to higher temperature for longer time duration have caused annihilation of deformation twins in the concerned case.

3.3.2. DRX grain size prediction

The kinetics of recrystallization can be mathematically related to the thermo-mechanical process parameters such as temperature and strain rate. The grain size during DRX can be approximated using the grain boundary migration theory put forth by Sandstrom [63], which can be further refined to obtain relationship between D_{DRX}, T, and strain rate as a phenomenological relationship between Ze and the D_{DRX}. Note that such relationships are sensitive to the hot deformation conditions. For instance, Li et al. [35], established a power law relationship between Ze and D_{DRX} for the processing conditions (0.0001–1 1/s, 250–550 °C) in the form
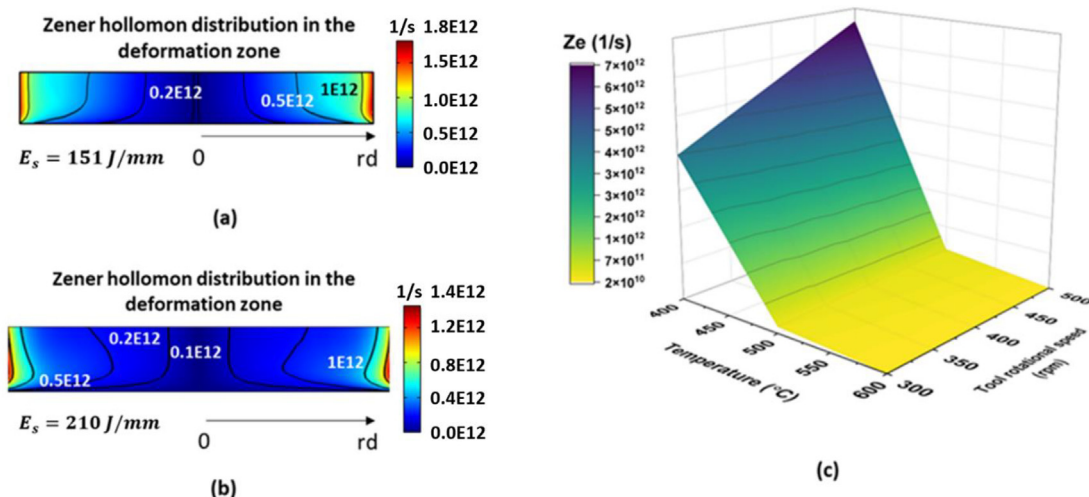
$$D_{DRX} = CZe^{\left(\frac{4}{n}-1\right)} \tag{14}$$

Fig. 14. Variation of Ze parameter in the deformation zone for (a) 151 J/mm and (b) 210 J/mm, (c) Ze-process map for AFSD of AZ31B. (For interpretation of the references to color in this figure legend, the reader is referred to the web version of this article.)
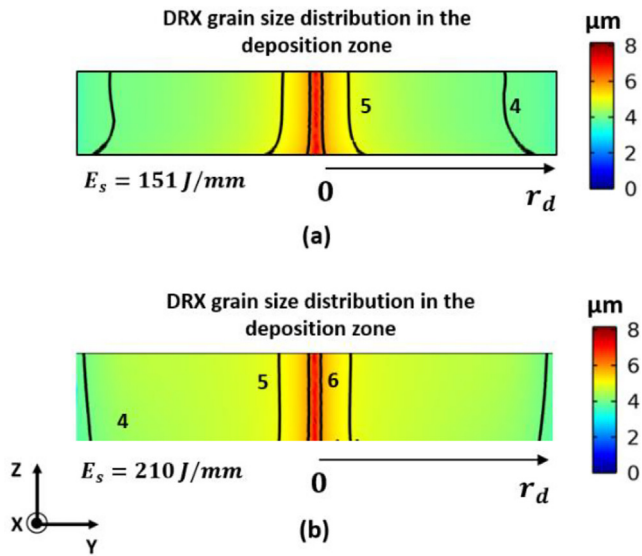
Fig. 15. D_{DRX} grain size evolution in deformation zone of (a) 151 J/mm and (b) 210 J/mm. (For interpretation of the references to color in this figure legend, the reader is referred to the web version of this article.)

Here C is a fitting constant whose value was in the range of 83–85 for above specified conditions, and the stress exponent n was evaluated to be 4.5. The proposed relationship measured well even in the case of high strain rate hot rolling and FSP conditions. Therefore, the above relationship was applied in the current work for the deformation zone based on the Ze values shown in Fig. 15. Accordingly, D_{DRX} grain size in the deformation zone varied from 4 to 6 μm for both the processing conditions.

In addition, the logarithmic relationship proposed for FSP of AZ31B [64] can be expressed as

$$\ln(D_{DRX}) = 6.0 - 0.17\ln(Ze) \tag{15}$$

To exemplify predicted D_{DRX} sizes during both AFSD processing conditions ($E_s = 210J/mm$ and $151J/mm$), the Ze processing maps were generated similar to that in Fig. 14 for the above-

mentioned relationships in Eqs. 14–15 and presented in Fig. 16 for the defined range of AFSD processing conditions ($E_s = 210J/mm$ and $151J/mm$) with D_{DRX} variation from 3 to 6 μm and 2–7 μm respectively). Turning back to grain size distribution presented in Fig. 10, it can be inferred that smaller grain sizes in Fig. 10 match well with the above prediction. Therefore, the presented pseudo-mechanical thermal model has the ability to predict not only thermal cycle but possible deformation mechanism and DRX grain size during the AFSD process.

3.3.3. Grain coarsening post deformation

In case of AFSD of AZ31B, the material after experiencing partial DRX exhibits inhomogeneous microstructure with 1) small and recrystallized grains with no apparent dislocations, 2) large and recrystallized grains with moderate dislocation density, and 3) uncrystallized grains with high dislocation density (KAM and GND maps in Fig. 11 and TEM micrograph in Fig. 12). Under such circumstances, when the material exits the deformation and deposition zone it is strain free. However, as predicted in the numerical as well as experimental results (Fig. 6 and Fig. 8), the material exiting the deposition zone experience thermal cycle with peak temperatures>400°C. In addition, the thermal cycle have low cooling rates (1–1 °C/s) estimated from numerical model which enables annealing of the deformed material for duration of several minutes (>3 min). These unique thermo-mechanical process conditions may result in considerable grain growth [65–67]. Naturally, each of the above-mentioned microstructural regions are likely to experience different static annealing behavior, especially at sustained temperature>400 °C. In literature, it has been postulated that under such unique processing condition, the degree of grain coarsening in AZ31B will strongly depend on the Ze parameter. For instance, Beer and Barnett [53], examined the dependence of grain coarsening during annealing of AZ31B post hot deformation. They reported presence of larger grain size when the material is processed with intermediate values of Ze. In their subsequent study of annealing of AZ31B at 350 °C post hot working conditions of (350 °C, 1 1/s), they observed rate of grain coarsening to saturate after 10 s. In the context of AFSD of AZ31B, the thermal cycle presented in Fig. 6, depicts repetitive heating and cooling cycle of duration>200 s. Therefore, it can be presumed that similar phe-
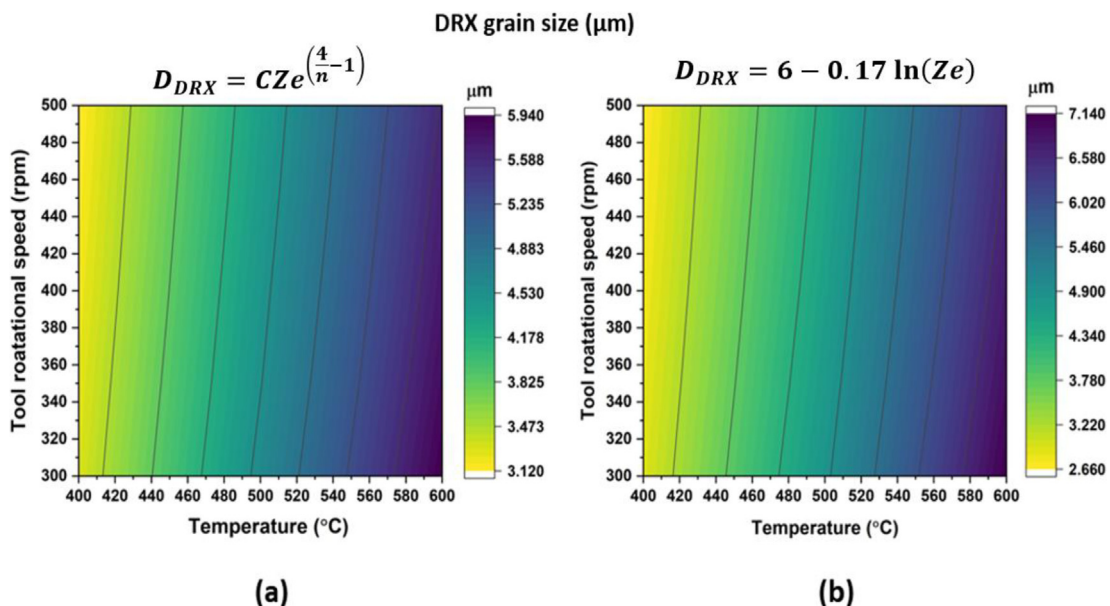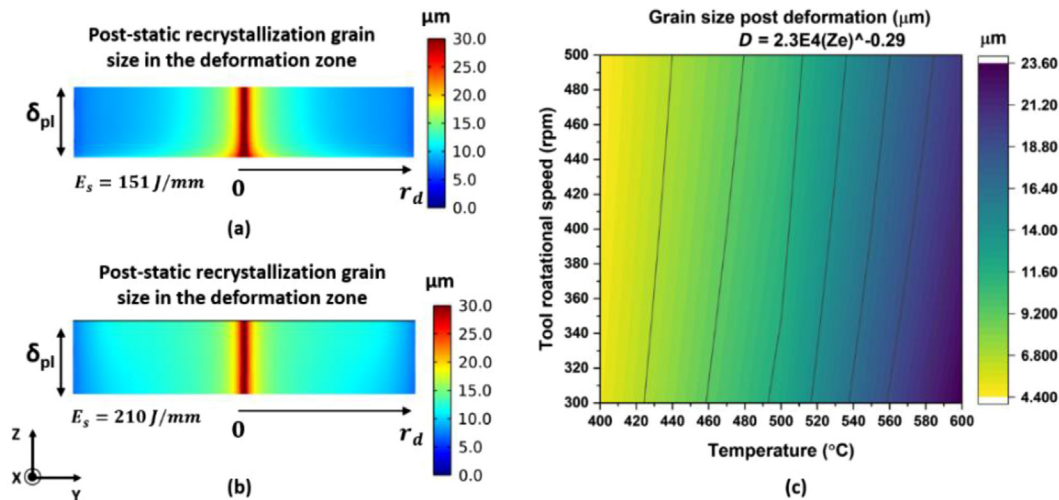

Fig. 16. Processing map of D_{DRX} variation with processing conditions for different phenomenological relationships of Ze. (For interpretation of the references to color in this figure legend, the reader is referred to the web version of this article.)

Fig. 17. Evolution of post-static recrystallization size in the deformation zone for (a) 151 J/mm, and (b) 210 J/mm, and (c) process map of post deformation grain size based Ze variation. (For interpretation of the references to color in this figure legend, the reader is referred to the web version of this article.)

nomena of grain coarsening may have occurred after deposition during AFSD as well. Following the above rationale, the phenomenological relationship between Ze and post-static recrystallization grain size proposed by Beer and Barnett [53] was incorporated in the present study. Such a Ze- post-static recrystallization grain size relationship can be expressed as

$$D = 2.3E4Ze^{-0.29} \tag{16}$$

The above relationship was considered in development of a Ze spatial map in the deformation zone for both the processing conditions ($E_s = 151J/mm \& 210J/mm and$) (Fig. 17 (a) and 17(b)). The predicted grain sizes are in the range of 6–24 μm, which agree reasonably well with grain size distribution depicted in Fig. 10. In addition, grain coarsening process map is depicted in Fig. 17 (c), which shows that under varying processing conditions of AFSD, the grain size varies from 4 to 24 μm. Note that the proposed relationship is based on processing conditions with strain rate of 1 1/s, which is significantly less than what is observed in AFSD. Nevertheless, the above results provide sufficient evidence towards preferential grain coarsening after AFSD deformation.

4. Conclusion

A novel multi-layer pseudo thermo-mechanical model linking process parameters to microstructural evolution has been developed for AFSD, a solid-state additive manufacturing process. The applicability of this model lies in its ability to predict the thermal profile, plausible deformation mechanisms, and post process grain size evolution. The predictions afforded by this model are in reasonable agreement with experiments. The computational run time for the 5-layer model was<20 min. Following are the main conclusions from the study -.

1. The computational thermal profiles obtained using frictional heating as well as heat generation due to plastic deformation matches well with the experimentally recorded thermal profiles. The peak temperature reached up to 0.8 Ts and was sensitive to change in tool rotational speed as well as linear travel speed. Further, it has been shown that consideration of only frictional heating in the mathematical model resulted in gross underestimation of the peak temperatures nearly by 100 °C.
2. The thermomechanical formulation in the deformation region provided important information pertaining to thermal evolu-

tion, strain rates, and state of stress during AFSD. It was observed that with increase in specific energy input from 151 J/mm to 210 J/mm, strain rate increased up to 400 1/s. The flow stress distribution was Centro-symmetric attaining peak value of 130 MPa near the periphery of deformation zone.
3. Microstructural evaluation suggested the occurrence of DRX followed by grain coarsening during AFSD of AZ31B. Further, with increase in specific linear energy density, the crystallographic texture exhibited strong basal fiber parallel to the ND axis
4. The imprint of unique thermo-mechanical processing conditions during AFSD of AZ31B have been elucidated with the theory of grain migration during DRX, phenomenological relationship between Ze and D_{DRX} was used to predict DRX grain size. The predicted grain size of 4–6 μm agrees well with experimental observations. Grain coarsening post deformation was also corelated with Ze parameter, and the predicted post deformation grain size of 4–24 μm agreed well with the experimental observations

Data availability

Data will be made available on request.

Declaration of Competing Interest

The authors declare that they have no known competing financial interests or personal relationships that could have appeared to influence the work reported in this paper.

Appendix A. Supplementary material

Supplementary data to this article can be found online at https://doi.org/10.1016/j.matdes.2022.111412.

References

[1] F. Khodabakhshi, A.P. Gerlich, Potentials and strategies of solid-state additive friction-stir manufacturing technology: A critical review, J. Manuf. Process. 36 (2018) 77–92, https://doi.org/10.1016/j.jmapro.2018.09.030.

[2] H.Z. Yu, R.S. Mishra, Additive friction stir deposition: a deformation processing route to metal additive manufacturing, Mater. Res. Lett. 9 (2021) 71–83, https://doi.org/10.1080/21663831.2020.1847211.

[3] R.S. Mishra, R.S. Haridas, P. Agrawal, Friction stir-based additive manufacturing, Sci. Technol. Weld. Join. 27 (2022) 141–165, https://doi.org/10.1080/13621718.2022.2027663.

[4] R.J. Griffiths, D. Garcia, J. Song, V.K. Vasudevan, M.A. Steiner, W. Cai, H.Z. Yu, Solid-state additive manufacturing of aluminum and copper using additive friction stir deposition: Process-microstructure linkages, Materialia (Oxf). 15 (2021), https://doi.org/10.1016/j.mtla.2020.100967 100967.

[5] B.J. Phillips, D.Z. Avery, T. Liu, O.L. Rodriguez, C.J.T. Mason, J.B. Jordon, L.N. Brewer, P.G. Allison, Microstructure-deformation relationship of additive friction stir-deposition Al–Mg–Si, Materialia (Oxf). 7 (2019), https://doi.org/10.1016/j.mtla.2019.100387 100387.

[6] H.B. Schmidt, J.H. Hattel, Thermal modelling of friction stir welding, Scr Mater. 58 (2008) 332–337, https://doi.org/10.1016/j.scriptamat.2007.10.008.

[7] H. Schmidt, J. Hattel, Modelling heat flow around tool probe in friction stir welding, Sci. Technol. Weld. Join. 10 (2005) 176–186, https://doi.org/10.1179/174329305X36070.

[8] P.A. Colegrove, H.R. Shercliff, R. Zettler, Model for predicting heat generation and temperature in friction stir welding from the material properties, Sci. Technol. Weld. Join. 12 (2007) 284–297, https://doi.org/10.1179/174329307X197539.

[9] C. Yang, C.S. Wu, L. Shi, Modeling the dissimilar material flow and mixing in friction stir welding of aluminum to magnesium alloys, J Alloys Compd. 843 (2020), https://doi.org/10.1016/j.jallcom.2020.156021 156021.

[10] M. Zhai, C.S. Wu, H. Su, Influence of tool tilt angle on heat transfer and material flow in friction stir welding, J Manuf Process. 59 (2020) 98–112, https://doi.org/10.1016/j.jmapro.2020.09.038.

[11] E. Hoyos, D. López, H. Alvarez, A phenomenologically based material flow model for friction stir welding, Mater Des. 111 (2016) 321–330, https://doi.org/10.1016/j.matdes.2016.09.009.

[12] A. Ajri, N. Rohatgi, Y.C. Shin, Analysis of defect formation mechanisms and their effects on weld strength during friction stir welding of Al 6061–T6 via experiments and finite element modeling, Int. J. Adv. Manuf. Technol. 107 (2020) 4621–4635, https://doi.org/10.1007/s00170-020-05353-3.

[13] V. Shokri, A. Sadeghi, M.H. Sadeghi, Thermomechanical modeling of friction stir welding in a Cu-DSS dissimilar joint, J Manuf Process. 31 (2018) 46–55, https://doi.org/10.1016/j.jmapro.2017.11.004.

[14] Q. Liu, R. Han, Y. Gao, L. Ke, Numerical investigation on thermo-mechanical and material flow characteristics in friction stir welding for aluminum profile joint, Int. J. Adv. Manuf. Technol. 114 (2021) 2457–2469, https://doi.org/10.1007/s00170-021-06978-8.

[15] G.G. Stubblefield, K. Fraser, B.J. Phillips, J.B. Jordon, P.G. Allison, A meshfree computational framework for the numerical simulation of the solid-state additive manufacturing process, additive friction stir-deposition (AFS-D), Mater Des. 202 (2021), https://doi.org/10.1016/j.matdes.2021.109514.

[16] E. Aghion, B. Bronfin, D. Eliezer, F. von Buch, S. Schumann, H. Friedrich, The art of developing new magnesium alloys for high temperature applications, Mater. Sci. Forum 419–422 (2003) 407–418, https://doi.org/10.4028/www.scientific.net/msf.419-422.407.

[17] L. Commin, M. Dumont, J.E. Masse, L. Barrallier, Friction stir welding of AZ31 magnesium alloy rolled sheets: Influence of processing parameters, Acta Mater. 57 (2009) 326–334, https://doi.org/10.1016/j.actamat.2008.09.011.

[18] T.-C. Wu, S.S. Joshi, Y.-H. Ho, M.V. Pantawane, S. Sinha, N.B. Dahotre, Microstructure and surface texture driven improvement in in-vitro response of laser surface processed AZ31B magnesium alloy, J. Magnesium Alloys 9 (4) (2021) 1406–1418.

[19] T.-C. Chang, J.-Y. Wang, C.-M. O, S. Lee, Grain refining of magnesium alloy AZ31 by rolling, J Mater Process Technol. 140 (1-3) (2003) 588–591.

[20] S.B. Yi, S. Zaefferer, H.G. Brokmeier, Mechanical behaviour and microstructural evolution of magnesium alloy AZ31 in tension at different temperatures, Mater. Sci. Eng. A 424 (2006) 275–281, https://doi.org/10.1016/j.msea.2006.03.022.

[21] S. Yi, J. Bohlen, F. Heinemann, D. Letzig, Mechanical anisotropy and deep drawing behaviour of AZ31 and ZE10 magnesium alloy sheets, Acta Mater. 58 (2010) 592–605, https://doi.org/10.1016/j.actamat.2009.09.038.

[22] S.R. Agnew, P. Mehrotra, T.M. Lillo, G.M. Stoica, P.K. Liaw, Crystallographic texture evolution of three wrought magnesium alloys during equal channel angular extrusion, Mater. Sci. Eng. A 408 (2005) 72–78, https://doi.org/10.1016/j.msea.2005.07.052.

[23] S.R. Agnew, Ö. Duygulu, Plastic anisotropy and the role of non-basal slip in magnesium alloy AZ31B, Int J Plast. 21 (2005) 1161–1193, https://doi.org/10.1016/j.ijplas.2004.05.018.

[24] S.M. Fatemi-Varzaneh, A. Zarei-Hanzaki, H. Beladi, Dynamic recrystallization in AZ31 magnesium alloy, Mater. Sci. Eng. A 456 (2007) 52–57, https://doi.org/10.1016/j.msea.2006.11.095.

[25] S.S. Joshi, S.M. Patil, S. Mazumder, S. Sharma, Additive friction stir deposition of AZ31B magnesium alloy, J. Magnesium Alloys (2022), https://doi.org/10.1016/j.jma.2022.03.011.

[26] D. Garcia, W.D. Hartley, H.A. Rauch, R.J. Griffiths, R. Wang, Z.J. Kong, Y. Zhu, H.Z. Yu, In situ investigation into temperature evolution and heat generation during additive friction stir deposition: A comparative study of Cu and Al-Mg-Si, Addit Manuf. 34 (2020), https://doi.org/10.1016/j.addma.2020.101386.

[27] X.M. Liu, Z.D. Zou, Y.H. Zhang, S.Y. Qu, X.H. Wang, Transferring mechanism of the coating rod in friction surfacing, Surf Coat Technol. 202 (2008) 1889–1894, https://doi.org/10.1016/j.surfcoat.2007.08.024.

[28] V.I. Vitanov, N. Javaid, Investigation of the thermal field in micro friction surfacing, Surf Coat Technol. 204 (2010) 2624–2631, https://doi.org/10.1016/j.surfcoat.2010.02.003.

[29] S.M. Bararpour, H. Jamshidi Aval, R. Jamaati, Modeling and experimental investigation on friction surfacing of aluminum alloys, J Alloys Compd. 805 (2019) 57–68, https://doi.org/10.1016/j.jallcom.2019.07.010.

[30] P. Li, J. Li, H. Dong, Analytical description of heat generation and temperature field during the initial stage of rotary friction welding, J Manuf Process. 25 (2017) 181–184, https://doi.org/10.1016/j.jmapro.2016.12.003.

[31] J.T. Xiong, L. Yuan, Y.J. Du, J.M. Shi, J.L. Li, The thermodynamic analytical models for steady-state of continuous drive friction welding based on the maximum entropy production principle, Appl Therm Eng. 159 (2019), https://doi.org/10.1016/j.applthermaleng.2019.113840.

[32] H. Schmidt, J. Hattel, J. Wert, An analytical model for the heat generation in friction stir welding, Model Simul, Mat Sci Eng. 12 (2004) 143–157, https://doi.org/10.1088/0965-0393/12/1/013.

[33] R. Nandan, G.G. Roy, T. Debroy, Numerical simulation of three dimensional heat transfer and plastic flow during friction stir welding, Metall Mater Trans A Phys Metall Mater Sci. 37 (2006) 1247–1259, https://doi.org/10.1007/s11661-006-1076-9.

[34] K.E. Tello, A.P. Gerlich, P.F. Mendez, Constants for hot deformation constitutive models for recent experimental data, Sci. Technol. Weld. Join. 15 (2010) 260–266, https://doi.org/10.1179/136217110X12665778348380.

[35] Y. Li, P. Hou, Z. Wu, Z. Feng, Y. Ren, H. Choo, Dynamic recrystallization of a wrought magnesium alloy: Grain size and texture maps and their application for mechanical behavior predictions, Mater Des. 202 (2021), https://doi.org/10.1016/j.matdes.2021.109562 109562.

[36] S. Spigarelli, M. el Mehtedi, M. Cabibbo, E. Evangelista, J. Kaneko, A. Jäger, V. Gartnerova, Analysis of high-temperature deformation and microstructure of an AZ31 magnesium alloy, Mater. Sci. Eng. A 462 (2007) 197–201, https://doi.org/10.1016/J.MSEA.2006.03.155.

[37] B.-H. Lee, K. Seon Shin, C. Soo Lee, B. Lee, K. Shin, C. Lee, High Temperature Deformation Behavior of AZ31 Mg Alloy, in: Material Science Forum, Trans Tech Publications, Switzerland, 2005. 10.4028/www.scientific.net/MSF.475-479.2927.

[38] K. Yu, Z. Cai, Y.U. Kun, Z.-Y. Cai, X.-Y. Wang, T. Shi, W.-X. Li, Constitutive analysis of AZ31 magnesium alloy plate metal matrix composites View project Constitutive analysis of AZ31 magnesium alloy plate, J. Cent. South Univ. Technol. 17 (2010) 7–12, https://doi.org/10.1007/s11771-010-0002-x.

[39] J. Qian, Y. Ou, J. Li, Y. Xiao, L. Wu, Y. Xu, An analytical model to calculate the peak temperature for friction stir welding, Sci. Technol. Weld. Join. 22 (2017) 520–525, https://doi.org/10.1080/13621718.2016.1268367.

[40] M. v. Pantawane, Y.H. Ho, S.S. Joshi, N.B. Dahotre, Computational Assessment of Thermokinetics and Associated Microstructural Evolution in Laser Powder Bed Fusion Manufacturing of Ti6Al4V Alloy, Scientific Reports 2020 10:1. 10 (2020) 1–14. 10.1038/s41598-020-63281-4.

[41] S.S. Joshi, S. Sharma, S. Mazumder, M. v. Pantawane, N.B. Dahotre, Solidification and microstructure evolution in additively manufactured H13 steel via directed energy deposition: Integrated experimental and computational approach, J Manuf Process. 68 (2021) 852–866. 10.1016/J.JMAPRO.2021.06.009.

[42] W. Hu, Q. Le, Z. Zhang, L. Bao, J. Cui, Numerical simulation of DC casting of AZ31 magnesium slab at different casting speeds, J. Magnesium Alloys 1 (2013) 88–93, https://doi.org/10.1016/j.jma.2013.02.010.

[43] J. Gandra, H. Krohn, R.M. Miranda, P. Vilaça, L. Quintino, J.F. dos Santos, Friction surfacing - A review, J Mater Process Technol. 214 (2014) 1062–1093, https://doi.org/10.1016/j.jmatprotec.2013.12.008.

[44] H. Khalid Rafi, K. Balasubramaniam, G. Phanikumar, K. Prasad Rao, Thermal profiling using infrared thermography in friction surfacing, Metall Mater Trans A Phys Metall Mater Sci. 42 (2011) 3425–3429, https://doi.org/10.1007/s11661-011-0750-8.

[45] Y. Jiang, L. Guan, G. Tang, Recrystallization and texture evolution of cold-rolled AZ31 Mg alloy treated by rapid thermal annealing, J Alloys Compd. 656 (2016) 272–277, https://doi.org/10.1016/J.JALLCOM.2015.09.155.

[46] M. Pareek, A. Polar, F. Rumiche, J.E. Indacochea, Metallurgical Evaluation of AZ31B-H24 Magnesium Alloy Friction Stir Welds, (n.d.). 10.1007/s11665-007-9084-5.

[47] J.-H. Park, T.-H. Ahn, H.-S. Choi, J.-M. Chung, D.-I. Kim, K.H. Oh, H.N. Han, Statistical Analysis on Static Recrystallization Texture Evolution in Cold-Rolled AZ31 Magnesium Alloy Sheet, (1927). 10.1017/S1431927613012257.

[48] R.D. Doherty, D.A. Hughes, F.J. Humphreys, J.J. Jonas, D. Juul Jensen, M.E. Kassner, W.E. King, T.R. McNelley, H.J. McQueen, A.D. Rollett, Current issues in

recrystallization: A review, Mater. Today 1 (1998) 14–15, https://doi.org/10.1016/s1369-7021(98)80046-1.

[49] S.S. Joshi, S. Sharma, M. Radhakrishnan, M. v. Pantawane, S.M. Patil, Y. Jin, T. Yang, D.A. Riley, R. Banerjee, N.B. Dahotre, A multi modal approach to microstructure evolution and mechanical response of additive friction stir deposited AZ31B Mg alloy, Scientific Reports 2022 12:1. 12 (2022) 1–15. 10.1038/s41598-022-17566-5.

[50] B.H. Lee, N.S. Reddy, J.T. Yeom, C.S. Lee, Flow softening behavior during high temperature deformation of AZ31Mg alloy, J Mater Process Technol. 187–188 (2007) 766–769, https://doi.org/10.1016/j.jmatprotec.2006.11.053.

[51] M. Sanjari, S.A. Farzadfar, I.H. Jung, E. Essadiqi, S. Yue, Influence of strain rate on hot deformation behaviour and texture evolution of AZ31B, Mater. Sci. Technol. 28 (2012) 437–447, https://doi.org/10.1179/1743284711Y.0000000080.

[52] Z.-M. Liu, S.-M. Xing, P.-W. Bao, N. Li, S.-Q. Yao, M.-L. Zhang, Characteristics of hot tensile deformation and microstructure evolution of twin-roll cast AZ31B magnesium alloys, Transactions of Nonferrous Metals Society of China (English Edition) 20 (5) (2010) 776–782.

[53] A.G. Beer, M.R. Barnett, Microstructure evolution in hot worked and annealed magnesium alloy AZ31, Mater. Sci. Eng. A 485 (2008) 318–324, https://doi.org/10.1016/j.msea.2007.08.001.

[54] S.H. Chowdhury, D.L. Chen, S.D. Bhole, X. Cao, P. Wanjara, Friction stir welded AZ31 magnesium alloy, Microstructure, texture, and tensile properties, Metall Mater Trans A Phys Metall Mater Sci. 44 (2013) 323–336, https://doi.org/10.1007/s11661-012-1382-3.

[55] M.L. Olguín-González, D. Hernández-Silva, M.A. García-Bernal, V.M. Sauce-Rangel, Hot deformation behavior of hot-rolled AZ31 and AZ61 magnesium alloys, Mater. Sci. Eng. A 597 (2014) 82–88, https://doi.org/10.1016/j.msea.2013.12.027.

[56] H.K. Kim, W.J. Kim, Microstructural instability and strength of an AZ31 Mg alloy after severe plastic deformation, Mater. Sci. Eng. A 385 (2004) 300–308, https://doi.org/10.1016/j.msea.2004.06.055.

[57] A.H. Ammouri, G. Kridli, G. Ayoub, R.F. Hamade, Relating grain size to the Zener-Hollomon parameter for twin-roll-cast AZ31B alloy refined by friction

stir processing, J Mater Process Technol. 222 (2015) 301–306, https://doi.org/10.1016/j.jmatprotec.2015.02.037.

[58] W. Tang, S. Huang, S. Zhang, D. Li, Y. Peng, Influence of extrusion parameters on grain size and texture distributions of AZ31 alloy, J Mater Process Technol. 211 (2011) 1203–1209, https://doi.org/10.1016/j.jmatprotec.2011.01.014.

[59] Y.V.R.K. Prasad, K.P. Rao, Processing maps for hot deformation of rolled AZ31 magnesium alloy plate, Anisotropy of hot workability, Materials Science and Engineering A. 487 (2008) 316–327, https://doi.org/10.1016/j.msea.2007.10.038.

[60] K. Ishikawa, H. Watanabe, T. Mukai, High temperature compressive properties over a wide range of strain rates in an AZ31 magnesium alloy, J Mater Sci. 40 (2005) 1577–1582, https://doi.org/10.1007/s10853-005-0656-1.

[61] B.M. Darras, A model to predict the resulting grain size of friction-stir-processed AZ31 magnesium alloy, J Mater Eng Perform. 21 (2012) 1243–1248, https://doi.org/10.1007/s11665-011-0039-5.

[62] X. Liu, J.J. Jonas, L.X. Li, B.W. Zhu, Flow softening, twinning and dynamic recrystallization in AZ31 magnesium, Mater. Sci. Eng. A 583 (2013) 242–253, https://doi.org/10.1016/j.msea.2013.06.074.

[63] R. Sandström, R. Lagneborg, A controlling factor for dynamic recrystallisation, Scr. Metall. 9 (1975) 59–65, https://doi.org/10.1016/0036-9748(75)90146-5.

[64] C.I. Chang, C.J. Lee, J.C. Huang, Relationship between grain size and Zener-Holloman parameter during friction stir processing in AZ31 Mg alloys, Scr. Mater. 51 (2004) 509–514, https://doi.org/10.1016/j.scriptamat.2004.05.043.

[65] Q. Miao, L. Hu, X. Wang, E. Wang, Grain growth kinetics of a fine-grained AZ31 magnesium alloy produced by hot rolling, J Alloys Compd. 493 (2010) 87–90, https://doi.org/10.1016/j.jallcom.2009.12.049.

[66] C.W. Su, L. Lu, M.O. Lai, Recrystallization and grain growth of deformed magnesium alloy, Phil. Mag. 88 (2008) 181–200, https://doi.org/10.1080/14786430701805566.

[67] A.J. Carpenter, A.R. Antoniswamy, J.T. Carter, L.G. Hector, E.M. Taleff, A mechanism-dependent material model for the effects of grain growth and anisotropy on plastic deformation of magnesium alloy AZ31 sheet at 450 C, Acta Mater. 68 (2014) 254–266, https://doi.org/10.1016/j.actamat.2014.01.043.